Greenland Ice Sheet to fall below its Holocene minimum size by 2300

Joshua Cuzzone

jcuzzone@ucla.edu

University of California, Los Angeles

Jason Briner

University at Buffalo https://orcid.org/0000-0002-8584-0978

Gerard Otiniano

University at Buffalo

Olivia Truax

University of Otago https://orcid.org/0000-0002-3194-5248

Elizabeth Thomas

University at Buffalo https://orcid.org/0000-0002-6489-7123

Eric Steig

University of Washington https://orcid.org/0000-0002-8191-5549

Gregory Hakim

University of Washington https://orcid.org/0000-0001-8486-9739

Joseph Tulenko

University of Buffalo

Mathieu Morlighem

Dartmouth College https://orcid.org/0000-0001-5219-1310

Nicole-Jeanne Schlegel

NOAA Geophysical Fluid Dynamics Laboratory https://orcid.org/0000-0001-8035-448X

Sophie Nowicki

University at Buffalo

Sudip Acharya

University of Buffalo

Jacob Anderson

Lamont-Doherty Earth Observatory, Columbia University

Lambert Caron

Jet Propulsion Laboratory, California Institute of Technology

Anne de Vernal

Université du Québec à Montréal https://orcid.org/0000-0001-5656-724X

Jacob Downs

University of Montana
Emilie Folie-Boivin
Université du Québec à Montréal
Ryan Fleetwood
University of Montana https://orcid.org/0009-0003-9078-010X
Holly Kyeore Han
Jet Propulsion Laboratory https://orcid.org/0000-0002-3819-5275
Jesse Johnson
University of Montana
Eric Larour
Jet Propulsion Laboratory/CalTech/NASA https://orcid.org/0000-0002-4009-4238
Ana Carolina Luzardi
University of Buffalo
Zilu Meng
University of Washington
Karlee Prince
University of Buffalo
Joerg Schaefer
Columbia University https://orcid.org/0000-0002-6358-7115
Margie Turrin
Lamont Doherty
Liza Wilson
University of Buffalo
Xiner Wu
University of Quebed, Montreal
Nicolas Young
Lamont-Doherty Earth Observatory of Columbia University https://orcid.org/0000-0002-5958-937X

Physical Sciences - Article

Keywords:

Posted Date: June 29th, 2026

DOI: https://doi.org/10.21203/rs.3.rs-9962320/v1

Additional Declarations: There is **NO** Competing Interest.

Greenland Ice Sheet to fall below its Holocene minimum size by 2300

Joshua K. Cuzzone[1*], Jason P. Briner[2], Gerard A. Otiniano[2], Olivia Truax[3], Elizabeth K. Thomas[2], Eric J. Steig[4], Gregory J. Hakim[4], Joseph P. Tulenko[2], Mathieu Morlighem[5], Nicole-Jeanne Schlegel[6], Sophie Nowicki[2], Sudip Acharya[2], Jacob Anderson[7], Lambert Caron[8], Anne de Vernal[10], Jacob Downs[9], Émilie Folie-Boivin[10], Ryan M. Fleetwood[9], Kyeore Han[8], Jesse Johnson[9], Eric Larour[8], Ana Carolina Luzardi[2], Zilu Meng[4], Karlee Prince[2], Joerg Schaefer[7], Margie Turin[7], Liza Wilson[2], Xiner Wu[10], Nicolás E. Young[7]

[1]Joint Institute for Regional Earth System Science and Engineering, University of California, Los Angeles, CA, USA

[2]Department of Geology, University at Buffalo, Buffalo, NY, USA

[3]Te Kura Aronukurangi School of Earth and Environment, University of Canterbury, Christchurch, New Zealand

[4]Department of Earth and Space Sciences, University of Washington, Seattle, WA, USA

[5]Department of Earth Sciences, Dartmouth College, Hanover, NH, USA

[6]NOAA/OAR Geophysical Fluid Dynamics Laboratory, Princeton, NJ, USA

[7]Lamont–Doherty Earth Observatory, Columbia University, New York, NY, USA

[8]Nasa Jet Propulsion Laboratory, Pasadena, CA, USA

[9]Department of Mathematical Sciences, University of Montana, Missoula MT, USA

[10] Université du Québec à Montréal, Geotop Research Center, Montréal, QC, Canada

*Corresponding author. Email: jcuzzone@ucla.edu

Abstract

The Greenland Ice Sheet (GrIS) is a major contributor to sea-level rise, yet its long-term response to sustained warmth remains uncertain[1,2,3]. The Holocene represents the most recent interval during which the GrIS experienced centuries of temperatures above preindustrial levels, providing a natural benchmark for assessing its sensitivity to prolonged warming[4,5]. However, reproducing the geologically constrained evolution of the GrIS throughout the Holocene has remained a persistent challenge for ice-sheet models[6,7]. Here we present GrIS simulations forced by paleoclimate reconstructions and evaluated against extensive geological constraints to reconstruct its evolution from the Holocene to 2300 CE. By simultaneously capturing multiple independent records of past ice-sheet change, our ensemble provides a robust foundation for future projections. Under current warming trajectories, the GrIS shrinks below its Holocene minimum extent and volume by 2300 CE, while mass loss rates exceed Holocene maxima and contribute 26–86 cm of sea-level equivalent. Continued warming drives a nonlinear expansion of

the ablation zone beyond its Holocene range, whereas substantial emissions reductions limit the sea-level contribution to approximately 10 cm. These results indicate that future warming may push the Greenland Ice Sheet beyond the range of states experienced during the Holocene.

Main Text

Quantifying the centennial-scale commitment of the Greenland Ice Sheet (GrIS) to sea-level rise remains a fundamental challenge in climate science. While satellite observations capture a quarter-century of accelerating mass imbalance, understanding long-term trajectories requires evaluating model simulations against geological evidence from periods of sustained warmth long before the historical era[1,2]. Accelerated warming in the Arctic[3,8], and evidence that the GrIS may exhibit threshold-like behavior with +1.5°C of global mean warming[9,10,11], have led to the hypothesis that the ice sheet already is committed to long-term mass loss[12], potentially contributing up to 7.4 m to global sea level[13] within the next 1000 years[14,15]. Constraining future trajectories of ice mass loss requires numerical ice-sheet simulations that translate a range of future climate trajectories into ice mass change[16]. Reconstructions of past ice-sheet history, when paired with ice-sheet modeling, provide context for present-day ice mass imbalance, and present an opportunity to validate model physics outside the range of ice-sheet behavior observed within the relatively short 50-year historical (satellite-era) record. Here, we leverage Holocene observations and ice-sheet model simulations to provide a rigorous data-model informed understanding of GrIS evolution from the Holocene to the future.

The Holocene represents the most recent geologic interval during which the GrIS experienced regional summer temperatures substantially (~2–5 °C) above pre-industrial levels and maintained over many centuries[4,5]. Geological reconstructions of ice-margin retreat, relative sea-level change, and ice-sheet thinning indicate that the GrIS underwent substantial mass loss in response to prolonged warm conditions ~11,000 to 6000 years ago, with cumulative contributions to global mean sea level estimated at 1–3 m[17,18]. While observational and modeling studies demonstrate that the GrIS can respond rapidly to interannual and decadal climate variability via changes in surface mass balance and outlet-glacier dynamics[1,19], ice-sheet models and theoretical analyses also show that the GrIS exhibits dynamic inertia, leading to continued ice loss even after atmospheric warming stabilizes or declines[9,20,21,22,23]. Recognition of these long response times has increasingly shifted the focus of the field toward quantifying centennial- to millennial-scale ice-sheet commitment[24], a perspective now reflected in community sea-level assessments coordinated through the Ice Sheet Model Intercomparison Project [ISMIP7;https://www.ismip.org/research/ismip7-protocol], which will extend simulations to 2300 CE. The Holocene provides a well-constrained record of GrIS evolution during prolonged warmth that is directly relevant for evaluating centennial- to millennial-scale ice-sheet commitment under future climate forcing.

Decades of research have improved our understanding of the GrIS extent during the Holocene (Fig. 1). While early models relied on indirect data such as relative sea-level records and ice-core thinning histories[17,25,26,27], newer datasets (e.g., PaleoGrIS[6]) provide direct constraints on ice-margin changes from 13–7 ka. Comparisons between these data and recent simulations[6,7] show that models substantially underestimate the magnitude and persistence of Holocene ice loss, suggesting missing processes or biases in climate forcing. A regional modeling study of southwest Greenland[18] driven by proxy-constrained climate reconstructions demonstrated that peak Holocene ice-loss rates were comparable to modern observations and could be exceeded under future warming scenarios. However, that analysis was limited to a single sector of the ice sheet, did not include ice–ocean interactions, and only examined future evolution through 2100 CE. Consequently, whether the Greenland Ice Sheet as a whole can reproduce geologically constrained Holocene change and how its future evolution compares with the full range of Holocene variability remain unresolved.

Data-constrained ice-sheet simulations

Here, we build on the regional modeling framework[18] by extending ice-sheet simulations to the entire GrIS, using the Ice-sheet and Sea-level System Model[29] (ISSM) initialized from the reconstructed early Holocene ice extent at 12.5 ka[6]. Our simulations span the Holocene through the contemporary period and are further extended using centennial-scale future climate projections based on a range of Shared Socioeconomic Pathways (SSPs), enabling continuous assessment of GrIS evolution through 2300 CE. In contrast to earlier work[18], we explicitly represent ice–ocean interactions using physically based parameterizations of submarine melting beneath floating ice and calving at marine termini (Methods). We incorporate an expanded range of available Holocene climate forcings[30,31,32,this study] and provide proxy-constrained reconstructions of spatially heterogeneous Holocene climate variability via an ensemble of 20 simulated GrIS Holocene histories (Methods; Extended Data Table 1).

Our multidisciplinary approach includes an expanded model–data comparison that integrates multiple independent constraints on GrIS evolution derived from geological field evidence and paleoclimate proxies, allowing for a robust evaluation of model skill and uncertainty across the ensemble (Methods). Our 20 simulations bracket the evolution of ice area through the Holocene (Fig. 1B). While some of our individual simulations depict changes in GrIS area that closely match available geological observations, others do not. Furthermore, while some simulations depict a time period with smaller-than-present ice area, consistent with field studies, others do not. We therefore use a broad suite of available geological observations of ice and climate history to evaluate the skill of our simulations. We apply seven criteria to assess simulation accuracy compared to observational benchmarks (Methods, Extended Data Table 2, Supplementary Information) that include geological reconstructions of ice-margin change, paleoclimate proxy constraints, and key features of Holocene ice evolution, including minimum extent, re-expansion, and present-day ice geometry. Our data-model assessment yields six simulations that stand out as being most consistent with observations (Extended Data Table 1), the ensemble median of which we consider to be a best estimate representation of GrIS evolution through the Holocene (Fig. 1B).

Centennial-scale change during the Holocene

Using our validated ensemble members, we examine simulated rates of ice mass change through the Holocene to quantify the magnitude and persistence of GrIS response to sustained warmth (Fig. 2A). Increases in summertime temperature from 12.5 to 11.5 ka initiated widespread ice retreat and mass loss. Elevated mass loss began around 11.6 ka at ~3×10^4 Gt century^{-1}, with some ensemble members simulating loss up to 4×10^4 Gt century^{-1}. This early Holocene period of mass loss persisted through ~8 ka, interrupted only briefly by a two-century period of modest mass gain associated with the 8.2 ka climate-change event[33]. After ~8 ka, rates of ice mass change again became negative before they eventually oscillated between centuries of minor mass gain and loss from ~6 ka to the preindustrial period. Our simulations reveal a pronounced spatial shift in GrIS mass loss, with northern basins accounting for ~75–85% of total loss during the earliest Holocene, followed by greater mass loss in more southern basins between 10 and 7 ka (Fig. 3). After ~6.5 ka, mass-loss variability became increasingly concentrated in western Greenland basins, which together accounted for ~60–75% of late-Holocene variability, while northern basin contributions diminished substantially. Furthermore, our simulations provide the best-informed depiction of the Holocene minimum extent yet available, a smaller-than-present configuration (showing a retracted northern margin by 10s of km) that is difficult to produce using glacial-geologic methods (Fig. 3B; Methods).

Historical and future ice-sheet change

We next relate Holocene GrIS change to contemporary and future ice mass loss. For 1850–2300 CE, the ice-sheet model is forced with output from the CMIP6 NCAR CESM2-WACCM model[34,35], which provides a continuous forcing through 2300 CE. While CESM2-WACCM exhibits high equilibrium climate sensitivity[36], it simulates significant spatial heterogeneity over Greenland; pronounced polar amplification in the north is partially offset by a strong AMOC response and subpolar North Atlantic cooling in the south[37,38]. These outputs range from the high-mitigation SSP1-2.6 pathway, where atmospheric CO_2 peaks near 450 ppm and declines to ~400 ppm by 2300 CE, to the fossil-fuel-intensive SSP5-8.5 scenario, where CO_2 exceeds 2000 ppm. These scenarios yield distinct future warming trajectories: GrIS-mean annual warming by 2300 CE ranges from ~0–1 °C under SSP1-2.6 to ~16 °C under SSP5-8.5 (Methods, Extended Data Fig. 1, Supplementary Information). Over the 20th century (1900–2000 CE), the simulated ice mass loss is 0.4×10^4 Gt century^{-1} (Fig. 2B). Simulated future mass loss increases strongly with the radiative forcing and associated warming of four possible future pathways (Fig. 2). Under the most optimistic pathway (SSP1-2.6), mass loss is highest this century and declines thereafter, approaching simulated 20th-century levels by 2300 CE, with mass loss rates remaining within the range of natural Holocene climate variability. On the other hand, for the high end-member SSP5-8.5 pathway, mass loss approaches 3.8×10^4 Gt century^{-1} by 2100 CE and accelerates to 24.7×10^4 Gt century^{-1} by 2300 CE, exceeding by tenfold the maximum ice-loss rates during the Holocene. Within these end members lie two intermediate pathways that approximate humanity's current trajectory[39] (SSP2-4.5 and SSP3-7.0). For these intermediate trajectories, we simulate mass loss during 2000–2100 CE of $2.1–3.1 \times 10^4$ Gt century^{-1} followed by pronounced centennial-scale acceleration thereafter, increasing to $4.6–18.7 \times 10^4$ Gt century^{-1} between 2200 and 2300 CE (Fig. 2B).

In the 20th century (1900–2000 CE), simulated mass loss is dominated (~30%) by the SE sector of Greenland, with substantial secondary contributions from the NW, SW, and NE sectors (~15–20% each), and comparatively minor input from the northernmost basin (NO) (Extended Data Fig. 2). This partitioning is broadly consistent with geodetic reconstructions indicating pronounced marginal thinning in southeast and northwest Greenland since the Little Ice Age[40]. In the future, mass loss remains multi-basin but shifts inland and toward western dominance over time (Fig. 3B). For example, during 2000–2100 CE, losses are broadly distributed (NE ~27%; other major basins ~15–20%) and concentrated along coastal margins, whereas by 2200–2300 CE the SW basin becomes dominant (~30%) as rising equilibrium line altitude (ELA) drives inland expansion of the ablation zone (Extended Data Fig. 2).

Our findings suggest the GrIS is approaching a fundamental state change. Despite experiencing multiple centuries of warmth during the early Holocene, the GrIS remained within a stable envelope of ELA and mass balance, as the ablation zone was largely confined to low-elevation, marginal regions (Fig. 3B; Fig. 4). Under current warming trajectories, however, the GrIS will depart from this historical regime and enter a state characterized by enhanced sensitivity of mass loss to rising ELA. This shift is most clearly expressed as an increase in the fraction of the ice sheet exposed to ablation as ELA rises. In future simulations, the relationship between the fraction of GrIS area below the ELA and ELA becomes increasingly nonlinear, especially under high emissions scenarios (Fig. 4). This non-linear relationship reflects the ice sheet hypsometry, where higher elevations encompass progressively larger areas, and is amplified by surface-mass-balance–elevation feedbacks as thinning lowers the ice surface into warmer conditions. In the current emissions trajectory, the fraction of the ice sheet subject to ablation reaches levels unprecedented relative to the Holocene as early as 2050 CE, as melt and thinning extend to higher elevations. The current emissions trajectory is therefore characterized by ice mass loss rates that are not only greater than any experienced in the Holocene, but also increase non-linearly in coming centuries (Fig. 4).

These results suggest that on our current trajectory, the GrIS will become smaller by 2300 CE than it was during its minimum Holocene phase (Fig. 5; Extended Data Fig. 3), and likely also the smallest it has been since the last interglacial optimum (Marine Isotope Stage 5e around 125,000 years ago). The Holocene pattern of mass loss was associated primarily with ice thinning in marginal areas of northern Greenland, whereas future projections indicate elevated ice thinning penetrating farther inland and across higher elevations (Fig. 3B; Fig. 4). In addition to the non-linear increases in mass loss discussed above, this transition has immediate physical consequences: the abandoned and now-buried Camp Century[41], which currently resides in the accumulation zone at 1900 m asl, is projected to be in the ablation zone by 2200 CE and will be melting towards the GrIS surface under both intermediate climate trajectories (Fig. 3B).

Holocene perspective on future sea-level rise

Our data-validated simulations spanning 12,500 years provide the most robust estimates of Holocene GrIS evolution currently available, resolving the mismatch between models and geological constraints[27,28]. Future Greenland ice loss exceeds the Holocene envelope for all future scenarios except SSP1-2.6. Our simulated ice loss by 2300 CE yields 26–86 cm of sea level equivalent (SLE) for intermediate scenarios, at a rate of contribution far surpassing that of the early Holocene, when a comparable amount of sea level rise took 1000 years (Fig. 5A). Importantly, limiting warming to SSP1-2.6 restricts SLE to ~10 cm at 2300 CE (1% of current GrIS volume; Fig. 5B), whereas high emissions (SSP5-8.5) produce up to ~1.4 m of SLE (19% of volume). These results demonstrate that the GrIS may enter a state of sustained and potentially self-amplifying mass loss within the range of plausible future climate scenarios.

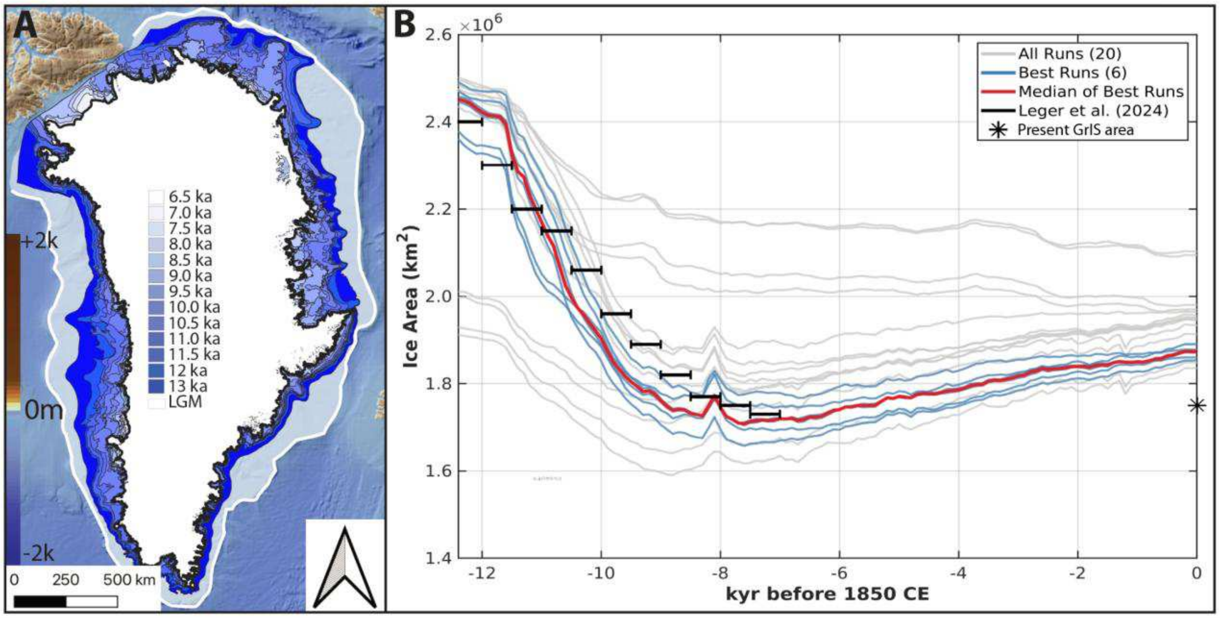

Fig. 1. Domain for Greenland Ice Sheet simulations and benchmark observations. A. Greenland model domain (13 ka polygon) and ice-sheet outlines guided by geological reconstructions[26]; after 6.5 ka, ice margins were within the present ice-sheet footprint. B. Results of simulation ensemble displaying evolution of ice-sheet area through the Holocene. Black horizontal bars are observations[26] of GrIS margin extent from panel A. The six best runs (evaluating fit against seven criteria from independent observations) are shown as blue lines with the median in red; 0 ka is 1850 CE.

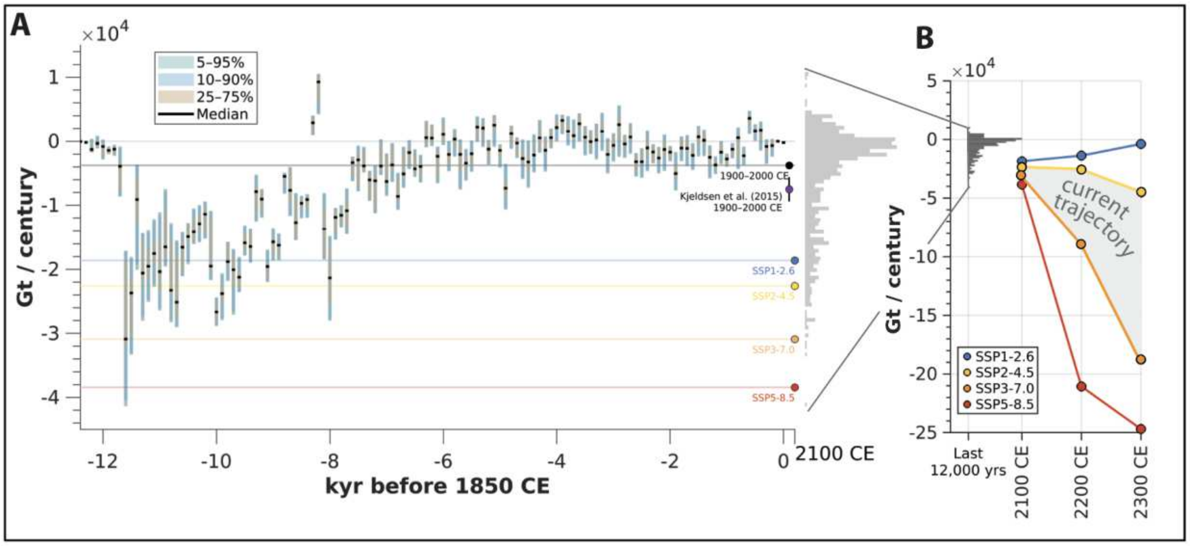

Fig. 2. Rates of ice-mass loss in the Holocene and near future. A. Rate of ice mass change spanning the Holocene, including the 20th century and a range of projections for the 21st century guided by SSP climate forcing; vertically-oriented histogram at right incorporates Holocene rates of ice-mass change from the best six runs (n = 720). B. Ice mass change per century for the next three centuries under four different SSP climate predictions; histogram at left is same as in A.

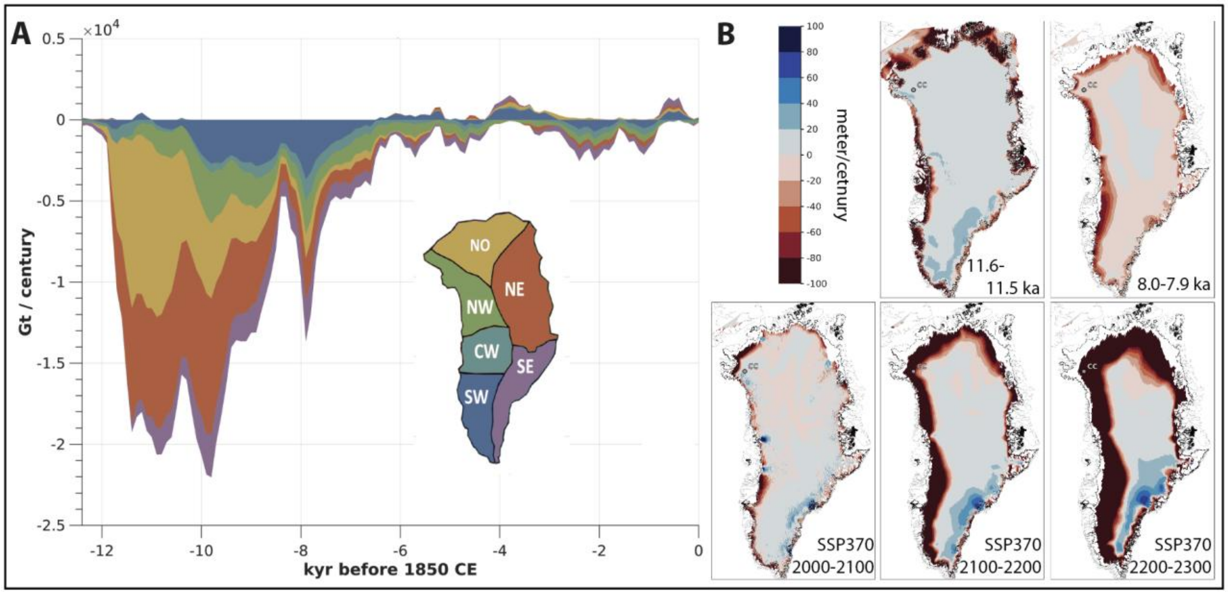

Fig. 3. Spatio-temporal patterns of ice-mass change on Greenland past and future. A. Simulated Holocene ice-mass change (after a 500-yr running mean was applied) partitioned by basin (inset); outer envelope of stacked domains is the grand sum. B. Simulated future ice-thickness changes (run 6; Extended Data Table 1) in the context of heavy ice-loss centuries in the Holocene. CC = Camp Century.

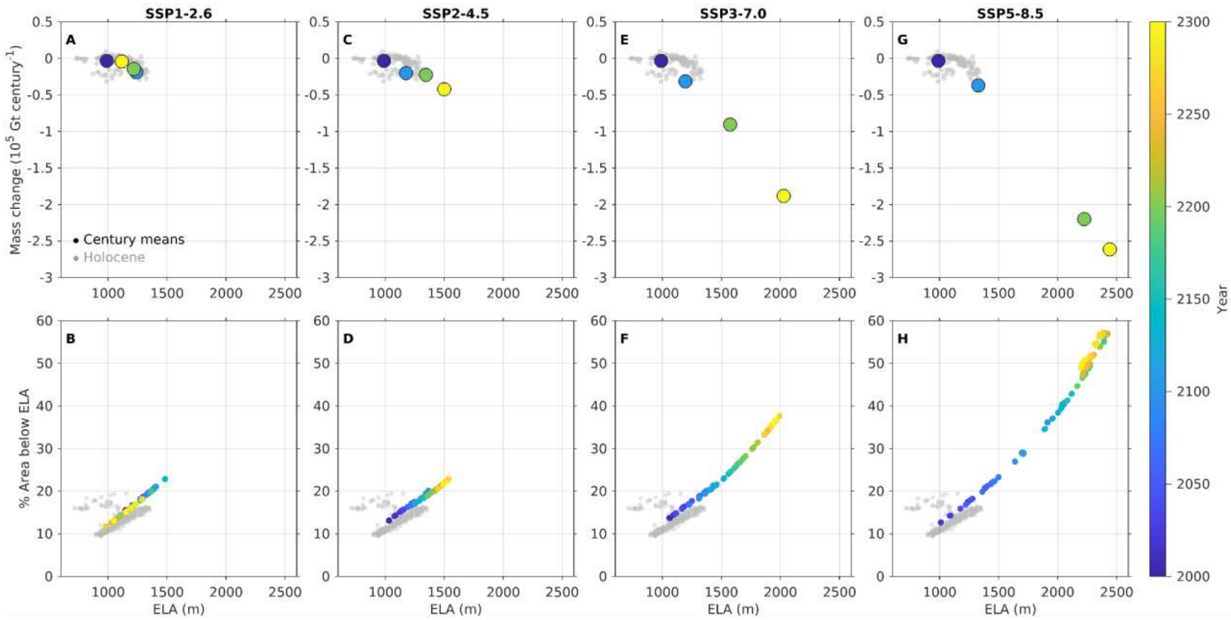

Fig. 4. Historical and future relationships between Equilibrium Line Altitude (ELA) and Greenland Ice Sheet (GrIS) mass balance. (**Top Row**) GrIS mass change (10^5 Gt century^{-1}) versus ELA (m) across four SSP warming scenarios. The grey background points indicate the Holocene envelope (12.5 ka to 1850 CE), during which the ablation zone was largely confined to marginal regions. The large, colored points represent century-scale averages for the 1900–1999, 2000–2099, 2100–2199, and 2200–2299 periods, respectively, with colors corresponding to the terminal year of each century. **(Bottom Row)** Percent area of the ice sheet subject to ablation (% area below ELA) versus ELA (m). Annual points are colored by year according to the shared colorbar. Grey background points indicate the Holocene constraint, where the area-below-ELA remained below ~20%. Future experiments reveal a non-linear, hypsometry-controlled increase in ablation area as the rising ELA moves inland and upward across higher ice tiers.

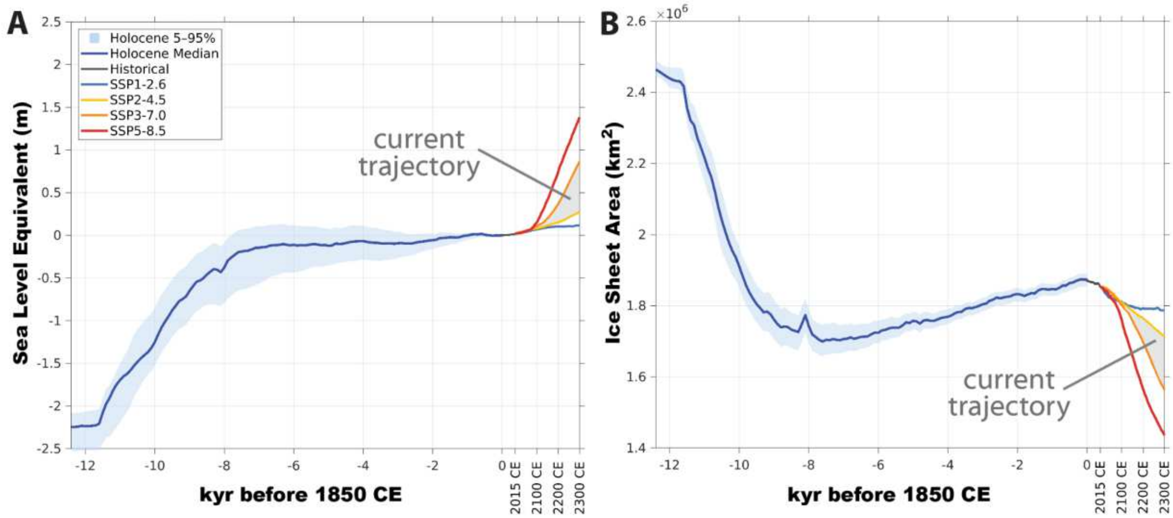

Fig. 5. Sea level rise and ice loss from Greenland in the context of the Holocene. A. Simulated contributions of sea level equivalent from Greenland spanning the Holocene and projected to the future when rates of sea level rise exceed the Holocene on the current climate trajectory. **B.** Simulated ice sheet area spanning the Holocene and future. Greenland Ice Sheet projected to be smaller by 2300 CE than any time in the Holocene and likely since ~125,000 yr ago.

Methods

Ice-sheet Model Description

To simulate the evolution of the GrIS across the Holocene and into the future, we use the finite element, thermomechanical Ice Sheet and Sea-level System Model (ISSM) v4.42[29]. The model domain follows the approximate geologically reconstructed 13–12 ka ice sheet boundary from PaleoGrIS version 1.0[28], which is extended to include the Nares Strait and a portion of Ellesmere Island that extends to the topographic divide (Extended Data Fig. 4). The initial bedrock topography is initialized from the BedMachine v3 product[13]. From this, we use anisotropic mesh adaptation to construct a non-uniform mesh that varies from 20 km in areas where gradients in bedrock topography are low to 1.5 km in areas where gradients in bedrock topography are high. Following from prior work[18,42,43,44], we prescribe glacial isostatic adjustment by using a reconstruction of relative sea level from a global GIA model of the last glacial cycle[45]. While GIA is not simulated transiently, we prescribe bedrock vertical motion, eustatic sea-level, and geoid change during the Holocene to account for GIA. For historical and future simulations (1850-2300 CE), bedrock topography remains fixed at present day conditions.

To solve the momentum-balance equations, we use a depth-integrated formulation of the high-order approximation[46]. In order to capture the time-evolving thermal state of the GrIS, we extrude our model to four layers and use an enthalpy formulation[47,48] that simulates both temperate and cold-based ice. The ice rheology follows Glen's flow law (n=3), with the ice viscosity being dependent on the simulated ice temperature following rate factors in[49], while the spatio-temporally varying surface temperature and the spatially variable (time constant) geothermal heat flux[50] are imposed as boundary conditions in the thermal model.

To compute the transient surface mass balance, we use a positive degree day method[51]. We use two combinations for the degree-day factors for snow and ice. Degree-day factors are 4 mm °C^{-1} d^{-1} and 8 mm °C^{-1} d^{-1} for snow and ice respectively, and 3 mm °C^{-1} d^{-1} and 6 mm °C^{-1} d^{-1} for snow and ice respectively. The formation of superimposed ice is accounted for following[52]. A lapse rate of 6 °C km^{-1} is used to adjust the temperature of the climate forcings onto the ice-surface elevation. These setups have been successfully applied in previous simulations of paleo GrIS change[18,53,54]. Basal sliding is parameterized using a linear viscous friction law following[55], $\tau_b = -k^2 N v_b$, in which the basal drag (τ_b) is proportional to basal velocity (v_b) and effective pressure (N). For these simulations, N evolves as the ice sheet thickness changes and is computed as ice overburden minus basal water pressure, $N = \rho_i g H - \rho_w g\,(-Z_b, 0)$, where g is gravity, H is ice thickness, ρ_i is the density of ice, ρ_w is the density of water, and Z_b is bedrock elevation relative to sea level, following[44]. Below sea level, basal water pressure is assumed hydrostatic; above sea level, basal water pressure is zero. The spatially varying friction coefficient k is derived using two methods that have been applied to paleo applications across Greenland before[18,53,54]. Using inverse methods[29,56], we derive the friction coefficient as the best match between modeled and derived modern surface velocities[57]. Since a large portion of our model domain extends outside of the present-day ice sheet extent, we derive the basal friction coefficient in these regions as a function of bedrock geometry following[58] where,

$$k = 200 \times \frac{[(0, z_b + 800), z_b]}{(z_h)}$$

This parameterization allows for higher basal friction coefficients across higher topographic relief and lower values across areas such as valleys and fjords. Throughout the simulations, the basal friction coefficient is adjusted following[42]. Where the basal temperature warms during the transient simulations relative to present day, the basal friction coefficient decreases, leading to increased sliding. Where the basal temperature cools during the simulation, the basal friction coefficient increases, leading to a reduction in sliding.

We track the migration of the ice-front using the levelset method[59],

$$v_f = v - (c + \dot{M})\, n,$$

which tracks the ice front velocity (v_f) as a function of the ice velocity vector at the ice front (v), the calving rate (c), the melting rate at the calving front ($\dot{M}$), and where n is the unit normal vector pointing horizontally outward from the calving front. For these simulations the melting rate is assumed to be negligible compared to the calving rate, so $\dot{M}$ is set to 0. The calving rate (c) is calculated based on the Von Mises stress calving approach[60], which relates the calving rate to the tensile stresses simulated within the ice as,

$$c = \|v\| \frac{\tilde{\sigma}}{\sigma_m}.$$

Here, $\tilde{\sigma}$ is the von Mises tensile strength, $\|v\|$ is the magnitude of the horizontal ice velocity, and σ_{max} is the maximum stress threshold which has separate values for grounded and floating ice. The ice front will retreat if von Mises tensile strength exceeds a user defined stress threshold, which we set to 200 kPa for floating ice and 1 MPa for tidewater ice. In these simulations, submarine frontal melt is not explicitly represented and is instead implicitly captured through a reduced calving threshold[53]. While this approach is appropriate for long-timescale paleo simulations, it does not account for potential changes in melt-driven undercutting and plume-enhanced melting under warmer climates, which may amplify outlet glacier retreat.

To compute sub-ice-shelf melt rates, we used the PICOP parameterization[61] within the ISSM framework. PICOP employs a box-model representation of sub-ice-shelf overturning circulation (PICO) coupled with a plume parameterization. This allows melt to be distributed locally as a function of thermal forcing, ice-shelf draft, and cavity slope. Ocean properties were prescribed to individual basins using six Greenland sectors delineated by the IMBIE-3[57] drainage basins (SE and CE were combined). Ambient temperature and salinity were extracted from the ECCO Version 4 Release 4[62] (V4r4) monthly reanalysis (1992–2010 mean) and sampled at a representative shelf depth of 450 m. This depth was chosen to approximate the influence of Atlantic Water (AW) at Greenland's marine-terminating margins. A key methodological choice was the decision not to impose time-evolving Holocene ocean temperature anomalies. While Sea

Surface Temperature (SST) reconstructions are available for the Holocene, they primarily reflect surface-layer polar water and sea-ice variability, which are often decoupled from the subsurface AW that drives grounding-line melt. Following consultation with palaeoceanographic experts (co-author A. de Vernal), it was determined that there are currently no well-constrained, centennial-to-millennial reconstructions of subsurface shelf-depth properties Greenland wide. By holding ocean thermodynamic properties constant across Holocene and Future, we avoid introducing structural uncertainty from poorly constrained paleo-anomalies. Consequently, temporal variability in our modeled melt rates arises solely from evolving ice geometry.

Model Experiments

Our ice sheet model experiments are run over 3 different time periods: Holocene (12,400 years ago to 1850 CE), historical (1850 – 2014 CE), and future (2015 – 2300 CE).

Initial State (12.5 ka):

We initialize our models with present-day ice-surface elevation from the Greenland Ice Mapping Project digital elevation model[63], and corresponding bedrock adjusted for GIA for the given time period[45]. For our simulations, we assume that the GrIS was in equilibrium with climate at 12.5 ka, with minor retreat during this interval[28]. To achieve this our relaxation procedure uses two steps following established procedures[18,44,53]. First, we take our 3D model and perform a thermomechanical steady-state calculation, imposing surface temperature (see ***Holocene climate boundary conditions***) as Dirichlet boundary to get an initial ice temperature and rheology in equilibrium with surface climate (i.e., convergence) following[48]. Second, we allow the ice sheet model to relax by imposing constant climate conditions at 12.5 ka, allowing the ice geometry and temperature to adjust and reach equilibrium.

Holocene climate reconstructions

We use spatially and temporally evolving surface temperature and snow accumulation estimates through the Holocene from previously published reconstructions[30,31,32], along with a new reconstruction developed as part of this work (Extended Data Fig. 5–7). One reconstruction[31] is based on temperature estimates from measurements of $\delta^{15}N$ of N_2 in ice-core air bubbles from central and northwest Greenland (GISP2, GRIP, and NEEM), derived using an inverse firn-densification modeling technique, bias corrected with the TraCE-21k transient climate-model simulations[64]. The second reconstruction[30] used a data-assimilation method, following[65], with TraCE-21k as the prior ensemble, and oxygen-isotope and snow-accumulation records from seven Greenland ice cores and the Agassiz Ice Cap core from the eastern Canadian Arctic, as the observational constraints. The third reconstruction[32] used a similar data-assimilation approach but assimilated global sea-surface temperature estimates from marine geochemical proxies. The prior ensemble used in the reconstruction[32] comprises time-slice simulations from the Community Earth System Model version 1[66].

Our new reconstruction is an update to the prior reconstruction[30], using a similar data-assimilation framework, with additional ice-core data and other modifications. We use the iCESM model time slices[32], and assimilate both the $\delta^{18}O$ and accumulation data[30], and the $\delta^{15}N$-based temperature data[31] as well as three new $\delta^{15}N$-based temperature reconstructions[67]. We directly assimilate $\delta^{18}O$ following published methods[68], rather than first converting isotope-ratios to temperature with linear scaling[30]. Unlike prior work[30,65], in which the prior is taken as a random draw from the climate-model simulations over all time periods, here, the prior ensemble changes through time to reflect known evolving orbital and greenhouse-gas forcing. We apply time-varying truncation bounds that prevent climatically implausible states from contributing to the prior at any given time step (e.g., model output from the Younger Dryas is not used as a prior for the Holocene). Additionally, we incorporate iCESM water-hosing experiments as an additional time-slice bin representing Younger Dryas boundary conditions, allowing the covariance structure to reflect the abrupt AMOC-driven cooling of that interval.

The four temperature reconstructions differ slightly in their treatment of seasonality. Three of the reconstruction methods provide annual-mean temperatures only. Seasonality is estimated by adding the orbitally-forced changes in seasonal amplitude through the Holocene from GCM simulations. Refs.[30,31] and our new reconstruction all use TraCE-21ka to provide the seasonality and spatial pattern. For our new reconstruction we lowpass-filter the TraCE-21ka seasonal cycle[18,30], whereas ref[31] retained the unsmoothed model seasonal cycle. Ref.[32] reconstructs seasonal change from the iCESM time-slice prior, which is built from discrete time intervals (e.g., 9ka, 6 ka) but samples continuously from the probability distribution of those slices, such that seasonality evolves through time. In all cases, the monthly temperature fields are interpolated onto the model mesh to construct the climate boundary conditions used in the ice-sheet simulations (***see Holocene climate boundary conditions section***). See Supplementary Information for methods used to correct and account for topography in paleoclimate reconstructions (Supplementary Note 1).

Together, available paleoclimate reconstructions provide an envelope of Greenland surface-temperature histories scenarios that effectively capture the range of uncertainties in the thermal climate forcing. We use the single temperature reconstructions from refs.[31,32], and our new reconstruction. We also use the Low and Moderate temperature scenarios from ref.[30], which reflect different assumptions about the magnitude of the linear $\delta^{18}O$-temperature relationship; in ref.[16] these provided better agreement between the geologic data and model simulations of Holocene ice retreat in SW Greenland than the High temperature scenario[30].

For precipitation, reconstructions are more limited than for temperature, and subject to uncertainties in dynamic thinning of the ice, necessary for converting measured ice-core layer thickness to net accumulation. Ref.[30] provides three different net precipitation scenarios, accounting for a range of plausible thinning histories. We adopt the Moderate and High scenarios (Extended Data Fig. 8), which differ primarily in the early- to mid-Holocene (in particular, the High scenario exhibits precipitation rates exceeding the 1850–2000 mean during the mid-Holocene).

Holocene climate boundary conditions (12.5 ka to 1850 CE; n = 20)

The simulations begin at the start of the Holocene and extend to the year 1850 CE. The precipitation (n = 2; High and Moderate scenario from ref.[30]) and temperature anomalies (n = 5; High and Moderate scenario from refs.[30,31,32] and this study) from the climate reconstructions are applied at 100-year temporal resolution, with the timing and amplitude changes during the Holocene varying between the reconstructions. The monthly mean output of temperature and precipitation from the reconstructions are expressed as anomalies from the 1850-2000 CE mean, with precipitation being expressed as a fraction of the mean 1850-2000 CE precipitation. Following[18,53,54], we apply these anomalies onto a higher-resolution basemap of monthly mean temperature and precipitation for the period 1850-2000 CE from[69]. Temperature and precipitation spanning the Holocene are given as:

$$T_t = \underline{T}_{(1850\text{–}2000)} + \Delta T_t \text{ and,}$$
$$P_t = \underline{P}_{(1850\text{–}2000)} \Delta P_t,$$

where $\underline{T}_{(1850\text{–}2000)}$ and $\underline{P}_{(1850\text{–}2000)}$ represent the monthly mean temperature and precipitation for the period AD 1850–2000 from (70) and ΔT_t and ΔP_t represent the monthly anomalies. For the Holocene experiments, we run an ensemble of 20 simulations summarized in Extended Data Table S1. These simulations use a combination of Holocene temperature forcings from the four paleoclimate reconstructions, two precipitation reconstructions from one of the paleoclimate reconstructions (see ***Holocene climate reconstructions***), and are run with two different combinations of degree-day factors for snow and ice melt (see ***Ice-sheet Model Description***). Our model domain shares a boundary with Ellesmere Island (Fig. S3) along the topographic divide. Here we impose transient Dirichlet boundary conditions of ice thickness across the Holocene at 500-year resolution from Ice-7G[70]. The ensemble members vary in simulated ice extent and volume at the start of the Holocene depending on the climate boundary conditions used. As the simulations continue across the Holocene, the climate boundary conditions vary along with the prescribed GIA. A summary of the simulations (n=20) and the accompanying boundary conditions are listed in Extended Data Table 1.

The Holocene simulations end at 1850 CE. From the ensemble of simulations (n = 20), we perform a multifactor model-data comparison (see ***Data-model comparison (DMC)***), to determine the best performing ensemble members. After this exercise, we are left with 6 simulations, from which we continue the historical and future simulations.

Historic simulations (1850 – 2014 CE; n = 6):

Our historical and future simulations rely on model output from the Community Earth System Model Version 2 (CESM2) Whole Atmosphere Community Climate Model (WACCM), herein referred to CESM2-WACCM[35, 71], which participated in ScenarioMIP[34]. We use monthly mean surface air temperature (*tas*) and precipitation flux (*pr*) and compute anomalies relative to the 1850–2000 CE mean. These anomalies are added onto our base 1850-2000 CE mean monthly climatology of[69] to maintain consistency with our Holocene and future projection framework. The 6 simulations (see Extended Data Table 1; Run# 2, 4, 6, 8, 18, 20) are then run from 1850 forward to 2014 CE.

Future simulations (2015 – 2300 CE CE; n = 6):

To simulate the evolution of the GrIS from 2015 to 2300 CE, we rely on climate model output from CESM2-WACCM[35]. This was chosen for its range of simulations which span multiple shared socioeconomic pathways (SSPs) and for consistency with the recommended climate model forcing for the latest Ice Sheet Model Intercomparison Project (ISMIP 7) protocol (https://www.ismip.org/research/ismip7-protocol). Similar to the historical simulations, we use monthly mean surface air temperature (*tas:* 2-meter reference height temperature) and precipitation flux (*pr*) and compute anomalies relative to the 1850–2000 CE mean. These anomalies are then added onto our base 1850-2000 CE mean monthly climatology of[69].

CESM2-WACCM output for SSP2-4.5 and SSP3-7.0 extends only to 2100 CE. To force the ice-sheet model through 2300 CE, we extended monthly temperature and precipitation anomalies beyond 2100 following a pattern-scaling approach[72] in which the late-century CESM spatial climate patterns are preserved while their amplitude evolves according to an extended global-mean trajectory. Because the magnitude and persistence of Arctic amplification after 2100 remain uncertain, we did not impose additional polar amplification or modify the simulated regional warming pattern. Instead, the extension was constrained by the evolution of global-mean temperature and precipitation anomalies, while preserving the internally consistent spatial structure of CESM2 in the late 21st century (Extended Data Figs. 1 and 9). See Supplementary Information for the full description of our method to extend temperature and precipitation forcings to 2300 CE (Supplementary note 2).

Data-model comparison (DMC)

We identified seven observation-based criteria for use in evaluating each of our 20 simulations. Some of our DMC criteria are more involved than others, and we outline our methodology for each in this section and the Supplementary Information (Supplementary note 3). We derived a scheme for each of the seven criteria that resulted in a score of 1 or a 0; we found that six individual simulations earned a 1 for at least six of the seven criteria (Extended Data Table 2). We leverage PaleoGRIS[28] both at the domain level regarding the spatio-temporal pattern of deglaciation (Supplementary Information Note 3 DMC-1), and on the total ice area trends (Supplementary Information Note 3 DMC-2). Other criteria weigh the agreement between the four climate reconstructions we use to drive our simulations with available climate proxy data (e.g. from lake sediments) that were not used in the reconstructions (Supplementary Information Note 3 DMC-3). We retain simulations that come closer to agreeing with the present-day ice area (Supplementary Information Note 3 DMC-4), and that exhibit a clear minimum ice extent followed by re-expansion (Supplementary Information Note 3 DMC-5) to be consistent with a large body of observational evidence from around the GrIS[72]. Additionally, we scrutinize the millennial-scale pattern of Gt/century oscillations in the SW GrIS domain for agreement with the well-dated moraine records in that region[73,74] following ref.[18] (Supplementary Information Note 3 DMC-6). Finally, we evaluate each simulation's history in northwest

Greenland against the recent discovery of the complete deglaciation and regrowth of Prudhoe Dome during the Holocene (Supplementary Information Note 3 DMC-7), a one-of-a-kind datapoint to constrain Holocene minimum ice extent[75]. See Supplementary Information for the full details of our seven DMC criteria, analysis, and results.

Data and materials availability:
Model outputs, paleoclimate reconstruction, spreadsheets of ice and mass change, and example code to load and extract data are deposited in the Dryad Digital Repository at http://datadryad.org/share/LINK_NOT_FOR_PUBLICATION/BbK3gM984qp4txbq3mR4vXi51QVVce7IgfboPNd4gxI. These data are currently private for peer review and will be publicly released immediately upon publication.

Code availability: Scripts to process model output are available at http://datadryad.org/share/LINK_NOT_FOR_PUBLICATION/BbK3gM984qp4txbq3mR4vXi51QVVce7IgfboPNd4gxI. The ISSM model used in this work is open-source and publicly available at https://issm.jpl.nasa.gov.

References

1. Mouginot, J., Rignot, E., Bjørk, A. A., van den Broeke, M., Millan, R., Morlighem, M., Noël, B., Scheuchl, B. & Wood, M. Forty-six years of Greenland Ice Sheet mass balance from 1972 to 2018. *Proc. Natl. Acad. Sci*. **116**, 9239–9244 (2019).

2. Otosaka, I. N., Horwarth, M., Mottram, R. & Nowicki, S. Mass balances of the Antarctic and Greenland ice sheets monitored from space. *Surv. Geophys*. **44**, 1615–1652 (2023).

3. IPCC. Climate Change 2021: The Physical Science Basis. Contribution of Working Group I to the Sixth Assessment Report of the Intergovernmental Panel on Climate Change (eds. Masson-Delmotte, V., Zhai, P., Pirani, A., Connors, S. L., Péan, C., Berger, S., Caud, N., Chen, Y., Goldfarb, L., Gomis, M. I., Huang, M., Leitzell, K., Lonnoy, E., Matthews, J. B. R., Maycock, T. K., Waterfield, T., Yelekçi, O., Yu, R. & Zhou, B.) (Cambridge Univ. Press, 2021).

4. Briner, J. P., McKay, N. P., Axford, Y., Bennike, O., Bradley, R. S., de Vernal, A., Fisher, D., Francus, P., Frechette, B., Gajewski, K., Jennings, A., Kaufman, D. S., Miller, G., Rouston, C. & Wagner, B. Holocene climate change in Arctic Canada and Greenland. *Quat. Sci. Rev*. **147**, 340–364 (2016).

5. Axford, Y., de Vernal, A. & Osterberg, E. C. Past warmth and its impacts during the Holocene thermal maximum in Greenland. *Annu. Rev. Earth Planet. Sci.* **49**, 279–307 (2021).

6. Leger, T. P. M., Ely, J. C., Clark, C. D., Bradley, S. L., Archer, R. E. & Zhu, J. Greenland Ice Sheet evolution over the last 24,000 years from model simulations. *The Cryosphere* **19**, 5719–5761 (2025).

7. Lauritzen, M. L., Solgaard, A., Rathmann, N. M., Vinther, B. M., Grindsted, A., Noël, B., Aðalgeirsdóttir, G. & Hvidberg, C. S. Modeled Greenland Ice Sheet evolution constrained by ice-core-derived Holocene elevation histories. *The Cryosphere* **19**, 3599–3622 (2025).

8. Rantanen, M., Karpechko, A. Y., Lipponen, A., Nordling, K., Hyvärinen, O., Ruosteenoja, K., Vihma, T. & Laaksonen, A. The Arctic has warmed nearly four times faster than the globe since 1979. *Commun. Earth Environ*. **3**, 168 (2022).

9. Robinson, A., Calov, R. & Ganopolski, A. Multistability and critical thresholds of the Greenland ice sheet. *Nat. Clim. Change* **2**, 429–432 (2012).

10. Armstrong McKay, D. I., Staal, A., Abrams, J. F., Winkelmann, R., Sakschewski, B., Loriani, S., Fetzer, I., Cornell, S. E., Rockström, J. & Lenton, T. M. Exceeding 1.5 °C global warming could trigger multiple climate tipping points. *Science* **377**, eabn7950 (2022).

11. Gutiérrez-González, L., Robinson, A., Alvarez-Solas, J., Tabone, I., Swierczek-Jereczek, J., Moreno-Parada, D. & Montoya, M. Hysteresis of the Greenland ice sheet from the Last Glacial Maximum to the future. *The Cryosphere* **20**, 1139–1162 (2026).

12. Stokes, C. R., Bamber, J. L., Dutton, A. & DeConto, R. M. Warming of +1.5 °C is too high for polar ice sheets. *Commun. Earth Environ*. **6**, 351 (2025).

13. Morlighem, M., Williams, C. N., Rignot, E., An, L., Arndt, J. E., Bamber, J. L., Catania, G., Chauché, N., Dowdeswell, J. A., Dorschel, B., Fenty, I., Hogan, K., Howat, I., Hubbard, A., Jakobsson, M., Jordan, T. M., Kjeldsen, K. K., Millan, R., Mayer, L., Mouginot, J., Noël, B. P. Y., O'Cofaigh, C., Palmer, S., Rysgaard, S., Seroussi, H., Siegert, M. J., Slabon, P., Straneo, F., van den Broeke, M. R., Weinrebe, W., Wood, M. & Zinglersen, K. B. BedMachine v3: Complete bed topography and ocean bathymetry mapping of Greenland. *Geophys. Res. Lett*. **44**, 11051–11061 (2017).

14. Paice, C. M., Fettweis, X. & Huybrechts, P. Positive feedbacks drive the Greenland ice sheet evolution in millennial-length MAR–GISM simulations under a high-end warming scenario. *The Cryosphere* **20**, 309–332 (2026).

15. Aschwanden, A., Fahnestock, M., Truffer, M., Brinkerhoff, D. J., Hock, R., Khroulev, C., Mottram, R. & Khan, S. A. Contribution of the Greenland Ice Sheet to sea level over the next millennium. *Sci. Adv.* **5**, eaav9396 (2019).

16. Nowicki, S. M. J., Goelzer, H., Abe-Ouchi, A., Aschwanden, A., Barthel, A., Calov, R., Chambers, C., Chegini, F., Gregory, J. M., Payne, H. J., Edwards, T. L., Robinson, A. S., Saito, F., Slater, A., Siegert, M. J., Huybrechts, P., Levermann, A., Lipscomb, J., Marzeion, G., Quiquet, A., van de Wal, R. S. W. & Winkelmann, R. Ice Sheet Model Intercomparison Project (ISMIP6) contribution to CMIP6. *Geosci. Model Dev.* **9**, 4521–4545 (2016).

17. Lecavalier, B. S., Milne, G. A., Simpson, M. J. R., Wake, L., Huybrechts, P., Tarasov, L., Kjeldsen, K. K., Funder, S., Long, A. J., Woodroffe, S. A., Dyke, A. S. & Larsen, N. K. A model of Greenland ice sheet deglaciation constrained by observations of relative sea level and ice extent. *Quat. Sci. Rev*. **102**, 54–84 (2014).

18. Briner, J. P., Cuzzone, J. K., Badgeley, J. A., Young, N. E., Morlighem, E. J., Schlegel, N.-J., Hakim, G. J., Schaefer, J. M., Lesnek, J. V., Thomas, E. K., Allan, E., Bennike, O., Cluett, A. A., Csatho, B., Downs, J., Larour, E. & Nowicki, S. Rate of mass loss from the Greenland Ice Sheet will exceed Holocene values this century. *Nature* **586**, 70–74 (2020).

19. Khan, S. A., Bjørk, A. A., Bamber, J. L., Morlighem, M., Bevis, M., Kjær, K. H., Mouginot, J., Løkkegaard, A., Holland, D. M., Aschwanden, A., Zhang, B., Helm, V., Korsgaard, N. J., Colgan, W., Larsen, N. K., Liu, L., Hansen, K., Barletta, V., Dahl-Jensen, T. S., Søndergaard, A. S., Csatho, B. M., Sasgen, I., Box, J. & Schenk, T. Centennial response of Greenland's three largest outlet glaciers. *Nat. Commun.* **11**, 5718 (2020).

20. Pattyn, F., Ritz, C., Hanna, E., Asay-Davis, X., DeConto, R., Durand, G., Favier, L., Fettweis, X., Goelzer, H., Golledge, N. R., Kuipers Munneke, P., Lenaerts, J. T. M., Nowicki, S., Payne, A. J., Robinson, A., Seroussi, H., Trusel, L. D. & van den Broeke, M. The Greenland and Antarctic ice sheets under 1.5 °C global warming. *Nat. Clim. Change* **8**, 1053–1061 (2018).

21. Bochow, N., Poltronieri, A., Robinson, A., Montoya, M., Rypdal, M. & Boers, N. Overshooting the critical threshold for the Greenland ice sheet. *Nature* **622**, 528–536 (2023).

22. Delhasse, A., Kittel, C. & Beckmann, J. Exploring the Greenland Ice Sheet's response to future atmospheric warming-threshold scenarios over 200 years. *The Cryosphere* **19**, 4459–4469 (2025).

23. Andernach, M., Kapsch, M. L. & Mikolajewicz, U. Stabilizing feedbacks allow for multiple states of the Greenland Ice Sheet in a fully coupled Earth system–ice sheet model. *The Cryosphere* **20**, 1047–1069 (2026).

24. Goelzer, H., Berends, C. J., Boberg, F., Durand, G., Edwards, T. L., Fettweis, X., Gillet-Chaulet, F., Glaude, Q., Huybrechts, P., Le Clec'h, S., Mottram, R., Noël, B., Olesen, M., Rahlves, C., Rohmer, J., van den Broeke, M. & van de Wal, R. S. W. Extending the range and reach of physically-based Greenland ice sheet sea-level projections. *The Cryosphere* **19**, 6887–6906 (2025).

25. Vinther, B. M., Buchardt, S. L., Clausen, H. B., Dahl-Jensen, D., Johnsen, S. J., Fisher, D. A., Koerner, R. M., Raynaud, D., Lipenkov, V., Andersen, K. K., Blunier, T., Rasmussen, S. O., Steffensen, J. P. & Svensson, A. M. Holocene thinning of the Greenland ice sheet. *Nature* 4**61**, 385–388 (2009).

26. Simpson, M. J. R., Milne, G. A., Huybrechts, P. & Long, A. J. Calibrating a glaciological model of the Greenland ice sheet from the Last Glacial Maximum to present-day using field observations of relative sea level and ice extent. *Quat. Sci. Rev*. **28**, 1631–1657 (2009).

27. Lecavalier, B. S., Fisher, D. A., Milne, G. A., Vinther, B. M., Tarasov, L., Huybrechts, P., Lacelle, D., Maine, B., Zheng, J., Bourgeois, J. & Dyke, A. S. High Arctic Holocene

temperature record from the Agassiz ice cap and Greenland ice sheet evolution. *Proc. Natl. Acad. Sci.* U.S.A. **114**, 5952–5957 (2017).

28. Leger, T. P. M., Clark, C. D., Huynh, C., Jones, S., Ely, J. C., Bradley, S. L., Diemont, C. & Hughes, A. L. C. A Greenland-wide empirical reconstruction of paleo ice sheet retreat informed by ice extent markers: PaleoGrIS version 1.0. *Clim. Past* **20**, 701–755 (2024).

29. Larour, E., Seroussi, H., Morlighem, M. & Rignot, E. Continental-scale, high-order, high spatial resolution ice sheet modeling using ISSM. *J. Geophys. Res. Earth Surf.* **117**, F01022 (2012).

30. Badgeley, J. A., Steig, E. J., Hakim, G. J. & Fudge, T. J. Greenland temperature and precipitation over the last 20,000 years using data assimilation. *Clim. Past* **16**, 1325–1346 (2020).

31. Buizert, C., Keisling, B. A., Box, J. E., He, F., Carlson, A. E., Sinclair, G. & DeConto, R. M. Greenland-wide seasonal temperatures during the last deglaciation. *Geophys. Res. Lett.* **45**, 1905–1914 (2018).

32. Osman, M. B., Tierney, J. E., Zhu, J., Tardif, R., Hakim, G. J., King, J. & Poulsen, C. J. Globally resolved surface temperatures since the Last Glacial Maximum. *Nature* **599**, 239–244 (2021).

33. Alley, R. B., Mayewski, P. A., Sowers, T., Stuiver, M., Taylor, K. C. & Clark, P. U. Holocene climatic instability: A prominent, widespread event 8200 yr ago. *Geology* **25**, 483–486 (1997).

34. O'Neill, B. C., Tebaldi, C., van Vuuren, D. P., Eyring, V., Friedlingstein, P., Hurtt, G., Knutti, R., Kriegler, E., Lamarque, J.-F., Lowe, J., Meehl, G. A., Moss, R., Riahi, K. & Sanderson, B. M. The Scenario Model Intercomparison Project (ScenarioMIP) for CMIP6. *Geosci. Model Dev.* **9**, 3461–3482 (2016).

35. Danabasoglu, G., Lamarque, J.-F., Bacmeister, J., Bailey, D. A., DuVivier, A. K., Edwards, J., Emmons, L. K., Fasullo, J., Garcia, R., Gettelman, A., Hannay, C., Holland, M. M., Large, W. G., Lauritzen, P. H., Lawrence, D. M., Lenaerts, J. T. M., Lindsay, K., Lipscomb, W. H., Mills, M. J., Neale, R., Oleson, K. W., Otto-Bliesner, B., Phillips, A. S., Sacks, W., Tilmes, S., van Kampenhout, L., Vertenstein, M., Bertini, A., Dennis, J., Deser, C., Fischer, C., Fox-Kemper, B., Kay, J. E., Kinnison, D., Kushner, P. J., Larson, V. E., Long, M. C., Mickelson, S., Moore, J. K., Nienhouse, E., Polvani, L., Rasch, P. J. & Strand, W. G. The Community Earth System Model Version 2 (CESM2). *J. Adv. Model. Earth Syst.* **12**, e2019MS001916 (2020).

36. Duffy, M. L., Simpson, I. R., Medeiros, B., Zhu, J., McCluskey, C. S., Herrington, A. R., Gettelman, A., Otto-Bliesner, B. L., Fasullo, J. T., Lauritzen, P. H., Neale, R. B. & Lawrence, D. M. Is the high ECS in CESM2 degrading transient climate change projections over the 21st century? *J. Adv. Model. Earth Syst.* **18**, e2025MS004967 (2026).

37. Bochow, N., Poltronieri, A. & Boers, N. Projections of precipitation and temperatures in Greenland and the impact of spatially uniform anomalies on the evolution of the ice sheet. *The Cryosphere* **18**, 5825–5863 (2024).

38. Meehl, G. A., Arblaster, J. M., Bates, S., Richter, J. H., Tebaldi, C., Gettelman, A., Medeiros, B., Bacmeister, J., DeRepentigny, P., Rosenbloom, N., Shields, C., Hu, A., Teng, H., Mills, M. J. & Strand, G. Characteristics of future warmer base states in CESM2. *Earth Space Sci.* **7**, e2020EA001296 (2020).

39. Hausfather, Z. An assessment of current policy scenarios over the 21st century and the reduced plausibility of high-emissions pathways. *Dialogues Clim. Change* **2**, 26–32 (2025).

40. Kjeldsen, K., Korsgaard, N., Bjørk, A. *et al.* Spatial and temporal distribution of mass loss from the Greenland Ice Sheet since AD 1900. *Nature* **528**, 396–400 (2015).

41. Colgan, W., Machguth, H., MacFerrin, M., Colgan, J. D., van As, D. & MacGregor, J. A. The abandoned ice sheet base at Camp Century, Greenland, in a warming climate. *Geophys. Res. Lett.* **43**, 8091–8096 (2016).

42. Cuzzone, J. K., Schlegel, N.-J., Morlighem, M., Larour, E., Briner, J. P., Seroussi, H. & Caron, L. The impact of model resolution on the simulated Holocene retreat of the southwestern Greenland ice sheet using the Ice Sheet System Model (ISSM). *The Cryosphere* **13**, 879–893 (2019).

43. Cuzzone, J. K., Romero, M. & Marcott, S. Modeling the timing of Patagonian Ice Sheet retreat in the Chilean Lake District from 22–10 ka. *The Cryosphere* **18**, 1381–1398 (2024).

44. Cuzzone, J. K., Barth, A., Barker, K. & Morlighem, M. Ice sheet model simulations reveal that polythermal ice conditions existed across the northeastern USA during the Last Glacial Maximum. *The Cryosphere* **19**, 1559–1575 (2025).

45. Caron, L., Ivins, E. R., Adhikari, S., Nilsson, J. & Blewitt, G. GIA model statistics for GRACE hydrology, cryosphere and ocean science. *Geophys. Res. Lett*. **45**, 2203–2212 (2018).

46. Dias dos Santos, T., Morlighem, M. & Brinkerhoff, D. A new vertically integrated mono-layer higher-order (MOLHO) ice flow model. *The Cryosphere* **16**, 179–195 (2022).

47. Aschwanden, A., Bueler, E., Khroulev, C. & Blatter, H. An enthalpy formulation for glaciers and ice sheets. *J. Glaciol.* **58**, 441–457 (2012).

48. Seroussi, H., Morlighem, M., Rignot, E., Khazendar, A., Larour, E. & Mouginot, J. Dependence of Greenland ice sheet projections on its thermal regime. *J. Glaciol.* **59**, 1024–1034 (2013).

49. Cuffey, K. M. & Paterson, W. S. B. *The Physics of Glaciers*. 4th edn. Amsterdam. Butterworth-Heinemann (2010).

50. Shapiro, N. M. & Ritzwoller, M. H. Inferring surface heat flux distribution guided by a global seismic model. *Earth Planet. Sci. Lett.* **223**, 213–224 (2004).

51. Tarasov, L. & Peltier, W. R. Impact of thermomechanical ice sheet coupling on a model of the 100 kyr ice age cycle. *J. Geophys. Res*. **104**, 9517–9545 (1999).

52. Janssens, I. & Huybrechts, P. The treatment of meltwater retention in mass-balance parameterizations of the Greenland ice sheet. *Ann. Glaciol.* **31**, 133–140 (2000).

53. Cuzzone, J. K., Young, N. E., Morlighem, M., Briner, J. P. & Schlegel, N.-J. Simulating the Holocene deglaciation across a marine-terminating portion of southwestern Greenland in response to marine and atmospheric forcings. *The Cryosphere* **16**, 2355–2372 (2022).

54. Barnett, J., Holmes, F. A., Cuzzone, J., Åkesson, H., Morlighem, M., O'Regan, M., Nilsson, J., Kirchner, N. & Jakobsson, M. Simulating the Holocene evolution of Ryder Glacier, North Greenland. *The Cryosphere* **19**, 3631–3653 (2025).

55. Budd, W. F. & Smith, I. N. The growth and retreat of ice sheets in response to orbital radiation changes. in *Sea Level, Ice, and Climatic Change* (ed. Allison, I.) 369–409 (IAHS Publication No. 131, 1981).

56. Morlighem, M., Rignot, E., Seroussi, H., Larour, E., Ben Dhia, H. & Aubry, D. Spatial patterns of basal drag inferred using control methods. *Geophys. Res. Lett.* **37**, L14502 (2010).

57. Rignot, E. & Mouginot, J. Ice flow in Greenland for the International Polar Year 2008–2009. *Geophys. Res. Lett.* **39**, L11501 (2012).

58. Åkesson, H., Morlighem, M., Nisancioglu, K. H., Svendsen, J. I. & Mangerud, J. Atmosphere-driven ice sheet mass loss paced by topography: Insights from modelling the south-western Scandinavian Ice Sheet. *Quat. Sci. Rev.* **195**, 32–47 (2018).

59. Bondzio, J. H., Seroussi, H., Morlighem, M., Kleiner, T., Rückamp, M., Humbert, A. & Larour, E. Y. Modelling calving front dynamics using a level-set method: Application to Jakobshavn Isbræ, West Greenland. *The Cryosphere* **10**, 497–510 (2016).

60. Morlighem, M., Bondzio, J., Seroussi, H., Rignot, E., Larour, E., Humbert, A. & Rebuffi, S. Modeling of Store Gletscher's calving dynamics, West Greenland. *Geophys. Res. Lett.* **43**, 2659–2666 (2016).

61. Pelle, T., Morlighem, M. & Bondzio, J. H. PICOP, a new ocean melt parameterization under ice shelves. *The Cryosphere* **13**, 1043–1049 (2019).

62. ECCO Consortium, Fukumori, I., Wang, O., Fenty, I., Forget, G., Heimbach, P. & Ponte, R. M. ECCO Central Estimate. Version 4 Release 4. https://doi.org/10.5067/ECCL4-ANC44 (2023).

63. Howat, I. M., Negrete, A. & Smith, B. E. The Greenland Ice Mapping Project (GIMP) land classification and surface elevation data sets. *The Cryosphere* **8**, 1509–1518 (2014).

64. Liu, Z., Otto-Bliesner, B. L., He, F., Brady, E. C., Tomas, R., Clark, P. U., Carlson, A. E., Lynch-Stieglitz, J., Curry, W. & Brook, E. Transient simulation of last deglaciation with a new mechanism for Bølling-Allerød warming. *Science* **325**, 310–314 (2009).

65. Hakim, G. J., Emile-Geay, J., Steiger, W. J. & Noone, D. M. Last Millennium Climate Reanalysis project: Framework and first results. *J. Geophys. Res. Atmos.* **121**, 6745–6764 (2016).

66. Brady, E., Stevenson, S., Bailey, D., Liu, Z., Noone, D., Nusbaumer, J., Otto-Bliesner, B. L., Tabor, C., Tomas, R., Wong, T., Zhang, J. & Zhu, J. The connected isotopic water cycle in the Community Earth System Model version 1. *J. Adv. Model. Earth Syst.* **11**, 2547–2566 (2019).

67. Martin, K. C., Buizert, C., Brook, E., Williams, O. L., Edwards, J. S., Riddell-Young, B., Fudge, T. J., Mederbel, F., Beaudette, R., Severinghaus, J., Oyabu, I., Kawamura, K., Kirk, M., Koldtoft, I., Steffensen, J. P. & Blunier, T. Greenland ice cores reveal a south-to-north difference in Holocene thermal maximum timings. *Geophys. Res. Lett.* **51**, e2024GL111405 (2024).

68. Steiger, N. J., Steig, E. J., Dee, S. G., Roe, G. H. & Hakim, G. J. Climate reconstruction using data assimilation of water isotope ratios from ice cores. *J. Geophys. Res. Atmos.* **122**, 1545–1568 (2017).

69. Box, J. E. Greenland ice sheet mass balance reconstruction. Part II: Surface mass balance (1840–2010). J. Clim. **26**, 6974–6989 (2013).

70. Roy, K. & Peltier, W. R. Relative sea level in the Western Mediterranean basin. *Quat. Sci. Rev.* **183**, 76–87 (2018).

71. Gettelman, A., Mills, M. J., Kinnison, D. E., Garcia, R. R., Smith, A. K., Marsh, D. R., Tilmes, S., Vitt, F., Bardeen, C. G., McInerny, J., Liu, H.-L., Solomon, S. C., Polvani, L. M., Emmons, L. K., Lamarque, J.-F., Richter, J. H., Glanville, A. S., Bacmeister, J. T., Phillips, A. S., Neale, R. B., Simpson, I. R., DuVivier, A. K., Hodzic, A. & Randel, W. J. The Whole Atmosphere Community Climate Model Version 6 (WACCM6). *J. Geophys. Res. Atmos.* **124**, 12380–12403 (2019).

72. Kjær, K. H., Pedersen, M. W., De Sanctis, B., De Cahsan, B., Korneliussen, T. S., Michelsen, C. S., Sand, K. K., Jelavić, S., Ruter, A. H., Schmidt, A. M. A., Kjeldsen, K. K., Tesakov, A. S., Snowball, I., Gosse, J. C., Alsos, I. G., Wang, Y., Dockter, C., Rasmussen, M., Jørgensen, M. E., Skadhauge, B., Prohaska, A., Kristensen, J. Å., Bjerager, M., Allentoft, M. E., Coissac, E., Rouillard, A., Simakova, A., Fernandez-Guerra, A., Bowler, C., Macias-Fauria, M., Vinner, L., Welch, J. J., Hidy, A. J., Sikora, M., Collins, M. J., Durbin, R., Larsen, N. K. & Willerslev, E. A 2-million-year-old ecosystem in Greenland uncovered by environmental DNA. *Nature* **612**, 283–287 (2022).

73. Young, N. E., Briner, J. P., Miller, G. H., Lesnek, A. J., Crump, S. E., Thomas, E. K., Pendleton, S. L., Cuzzone, J., Lamp, J., Zimmerman, S., Caffee, M. & Schaefer, J. M. Deglaciation of the Greenland and Laurentide ice sheets interrupted by glacier advance during abrupt coolings. *Quat. Sci. Rev.* **229**, 106091 (2020).

74. Lesnek, A. J., Briner, J. P., Young, N. E. & Cuzzone, J. K. Maximum southwest Greenland ice sheet recession in the early Holocene. *Geophys. Res. Lett.* **47**, e2019GL083164 (2020).

75. Walcott-George, C. K., Brown, N. D., Briner, J. P., Balter-Kennedy, A., Young, N. E., Kuhl, T., Moravec, E., Anandakrishnan, S., Stevens, N. T., Keisling, B., DeConto, R. M., Gkinis, V., MacGregor, J. A. & Schaefer, J. M. Deglaciation of the Prudhoe Dome in northwestern Greenland in response to Holocene warming. *Nat. Geosci.* **19**, 189–194 (2026).

Acknowledgements: We thank Matthew Osman for providing gridded outputs of Holocene monthly temperature for this work.

Funding:
National Science Foundation Arctic System Sciences award #2106971 (JPB, EKT, SN and JKC)

National Science Foundation Arctic System Sciences award #2105908 (NEY and JMS)

National Science Foundation Arctic System Sciences award #2107605 (JJ)

National Science Foundation Arctic System Sciences award #2105960 (MM)

National Science Foundation Arctic System Sciences award #2105805 (EJS, GJH)

National Aeronautics and Space Administration Cryosphere Program award #281945.02.53.04.87 (EL, N-JS, LC).

Author contributions:

Conceptualization: JKC, JPB, EKT, EJS, GJH, MM, SN, JJ, JS, NEY
Methodology: JKC, JPB, OT, GAO, EKT, EJS, GJH, JPT, N-JS, MM
Investigation: JKC, JPB, OT, GAO, EKT, EJS, GJH, JPT, MM, N-JS, SN, SA, JA, LC, AdV, JD, EF-B, RMF, KH, JJ, EL, ACL, ZM, KP, JS, MT, LW, XW, NEY
Visualization: JKC, JPB, GAO, EKT, JPT
Funding acquisition: JKC, JPB, EKT, EJS, GJH, MM, SN, JJ, JS, NEY, EL
Project administration: JKC, JPB, EKT, EJS, GJH, MM, SN, JJ, JS, NEY
Supervision: JKC, JPB, EKT, EJS, GJH, SN, JJ, AdV
Writing – original draft: JKC, JPB, EKT, GAO, JPT, EJS, GJH, OT
Writing – review & editing: JKC, JPB, OT, GAO, EKT, EJS, GJH, JPT, MM, N-JS, SN, SA, JA, LC, AdV, JD, EF-B, RMF, KH, JJ, EL, ACL, ZM, KP, JS, MT, LW, XW, NEY

Competing interests: The authors declare no competing interests.

Extended data figures and tables

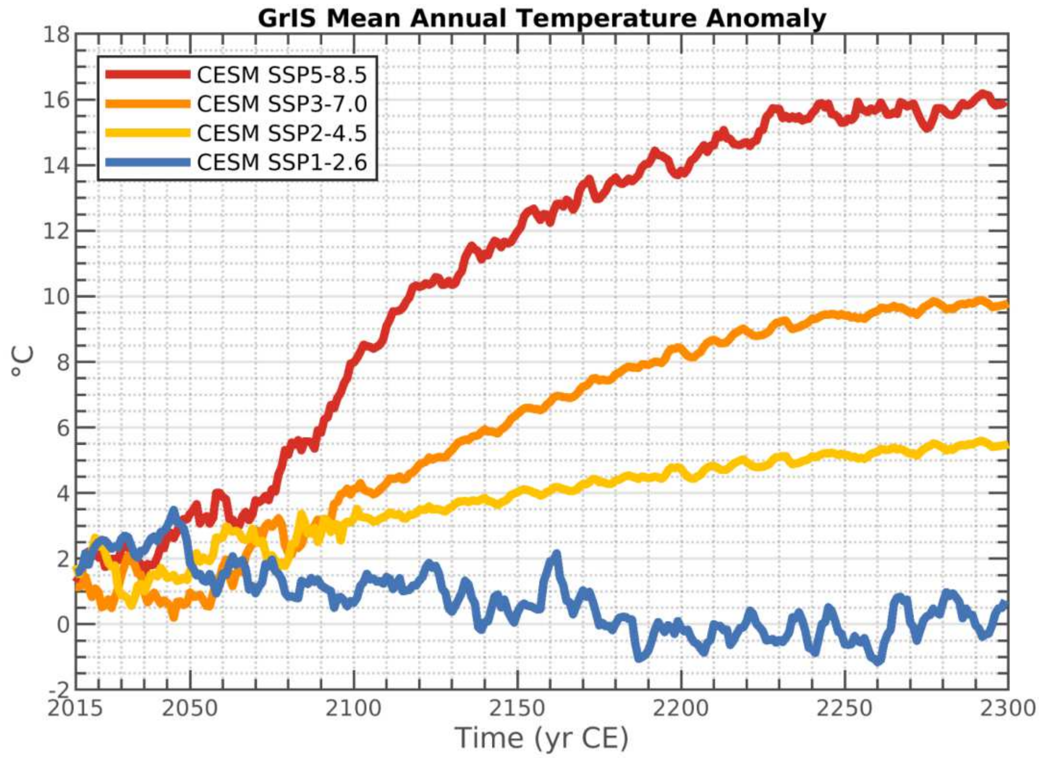

Extended Data Fig. 1: GrIS mean annual temperature anomaly for all 4 SSP scenarios
Future mean annual temperature expressed as an anomaly from the mean 1850-2000 CE period, for each SSP scenario.

905

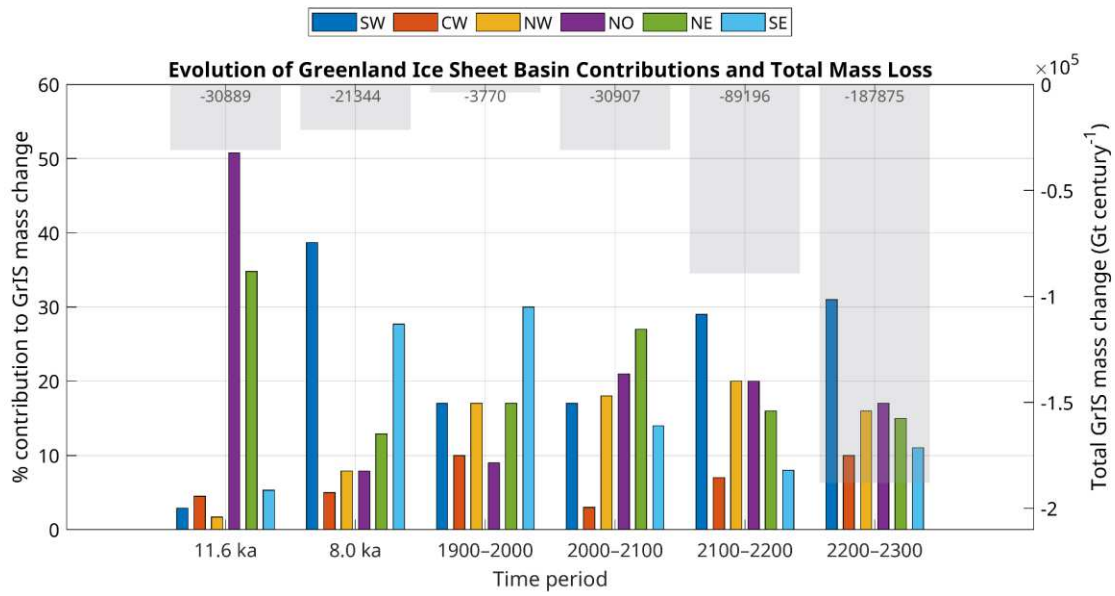

Extended Data Fig. 2: GrIS basin average contribution to Holocene and Future change
Contribution to GrIS change by each basin (in percent; y axis left) for high Holocene mass loss periods (11.6 and 8.0 ka), the historical period of 1900-2000, and the future following the SSP3-7.0 scenario. On the top of the figure is the corresponding century scale mass change in GT/century (y axis right).

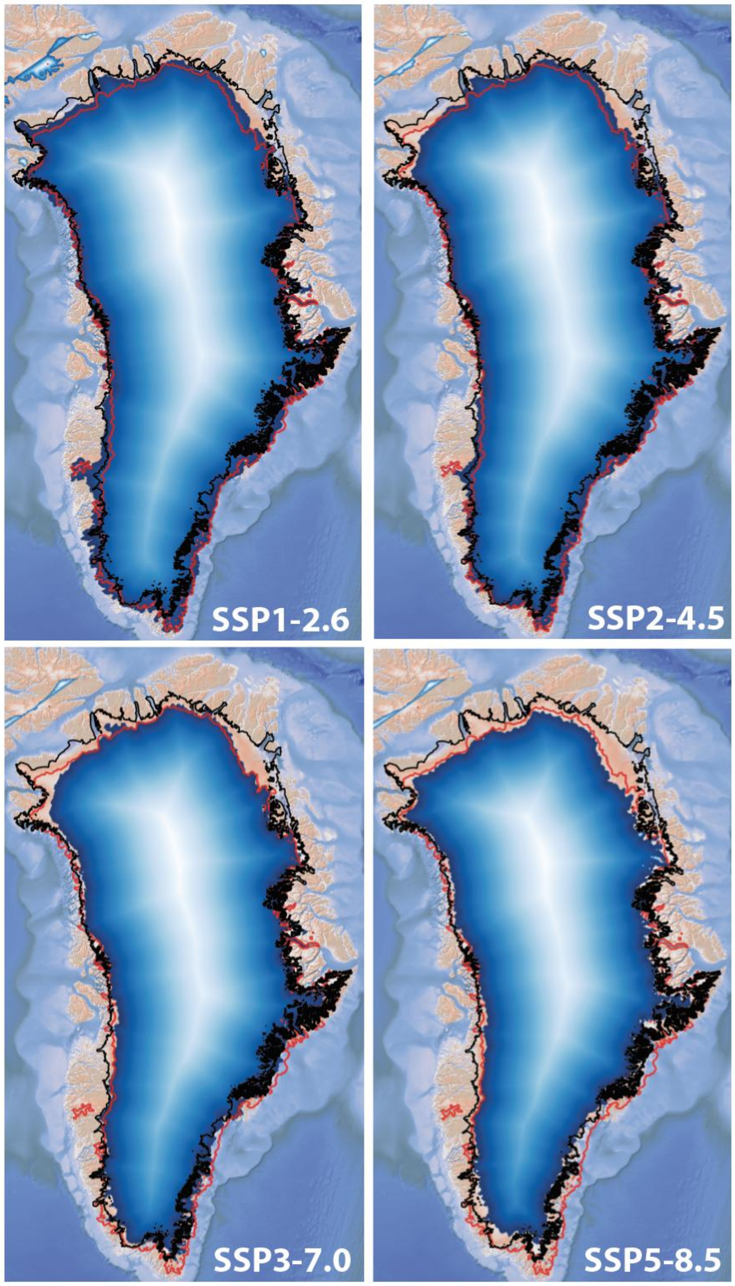

Extended Data Fig. 3: Simulated spatial ice extent of GrIS for Holocene and future scenarios

Simulated ice extent (for Run #6; see Extended Data Table 1) shown in blue at 2300 CE for four future climate trajectories. The red outline denotes the Holocene minimum ice extent for Run #6 (see Extended Data Table 1). The black outline corresponds to the present day ice extent[13].

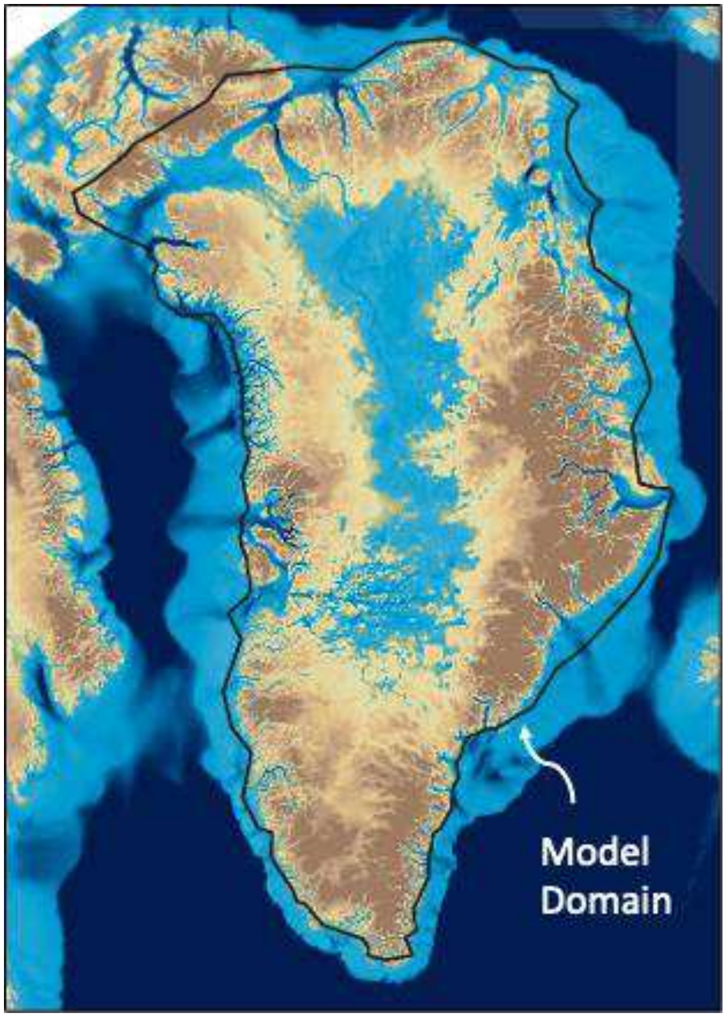

Extended Data Fig. 4: GrIS Model Domain
Ice-sheet model domain. The ice-sheet model domain is shown as the black contour and follows the approximate location of the 12.5 ka GrIS extent boundary from ref.[28].

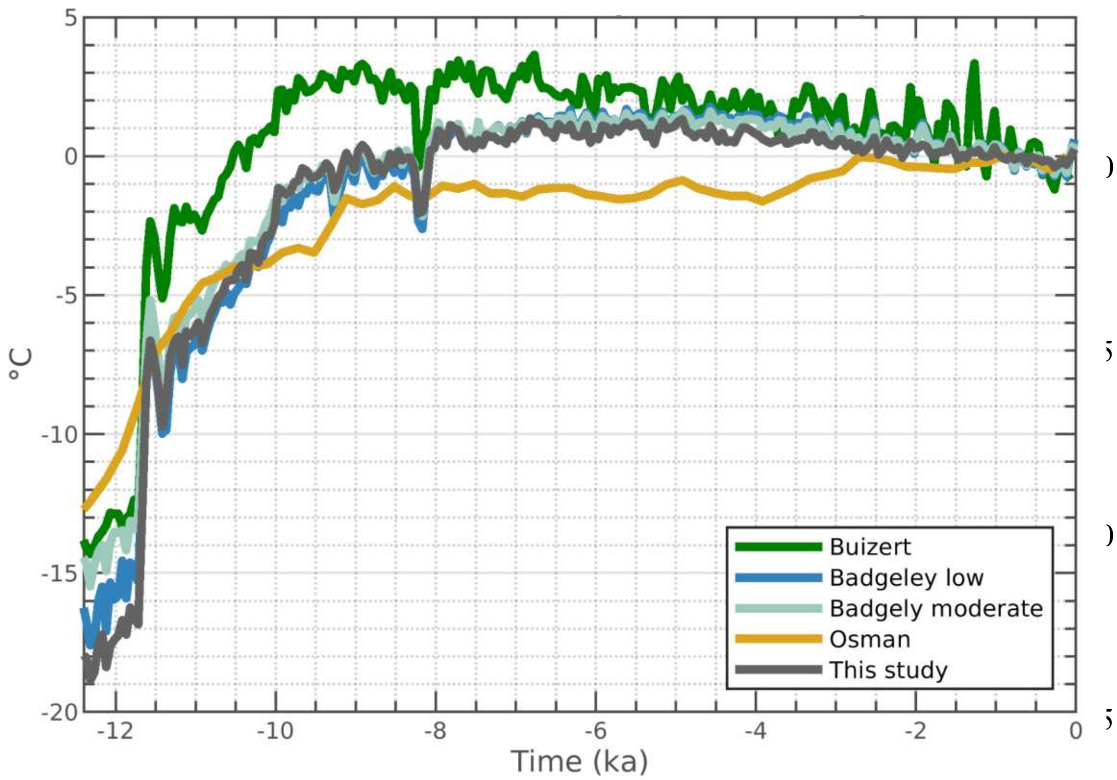

Extended Data Fig. 5: Reconstructed Holocene mean annual temperature
Reconstructed mean annual Holocene temperature for each reconstruction from refs.[30,31,32] and this study, expressed as an anomaly from the 1850-2000 mean from ref[69].

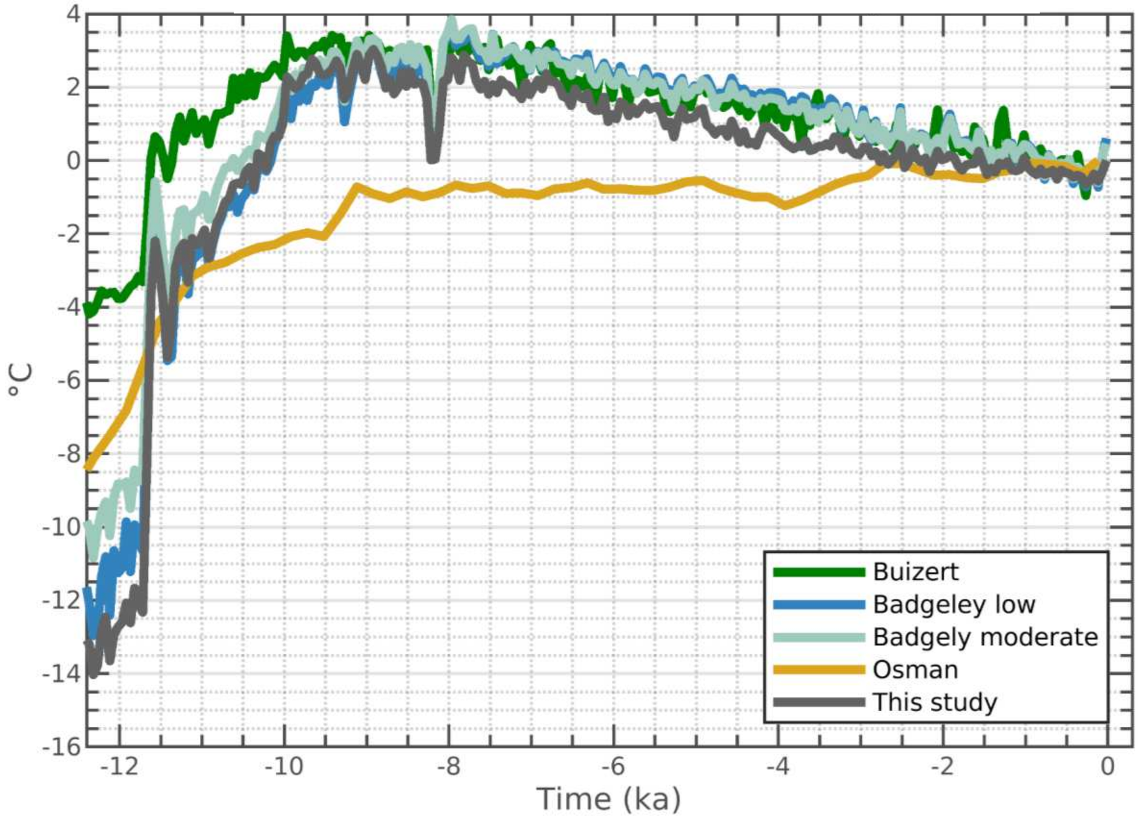

Extended Data Fig. 6: Reconstructed Holocene mean summer (JJA) temperature
Reconstructed mean Holocene summer (JJA) temperature for each reconstruction forom refs.[30,31,32] and this study, expressed as an anomaly from the 1850-2000 mean from ref.[69].

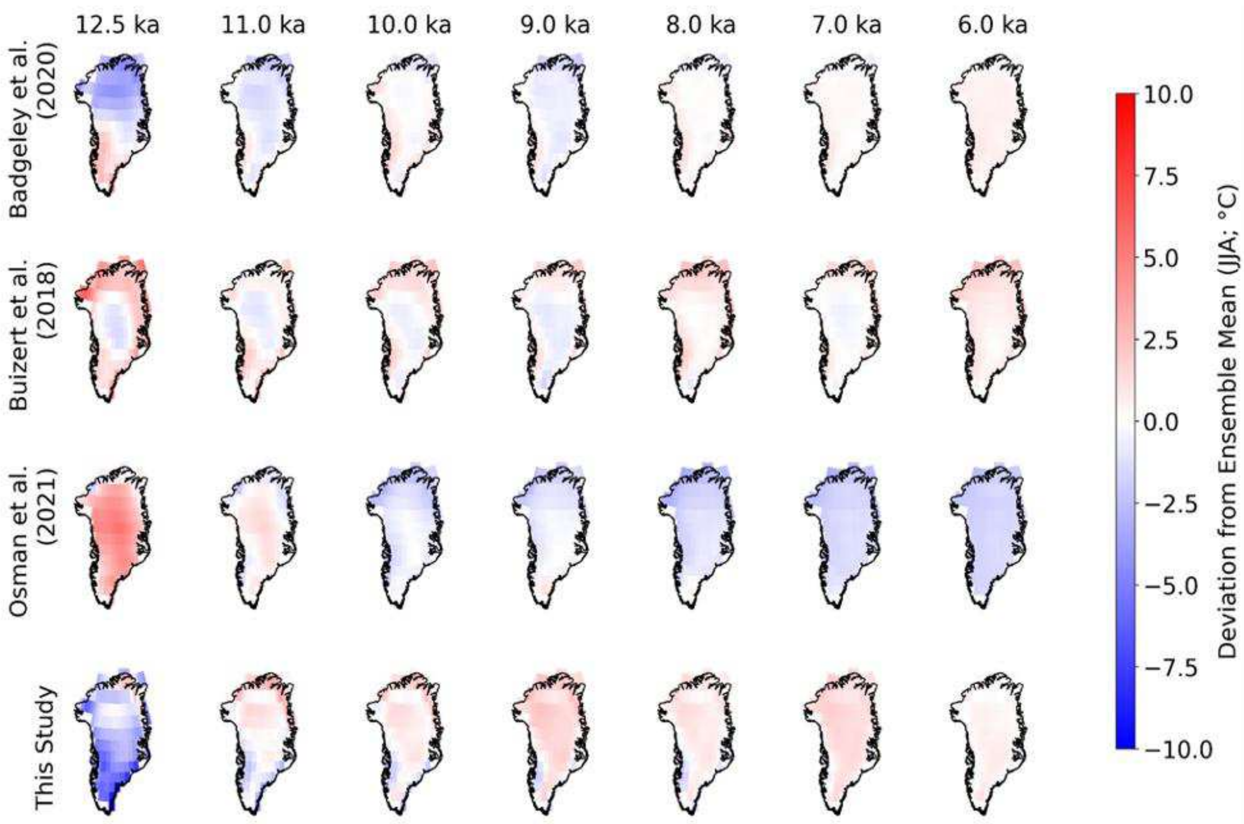

Extended Data Fig. 7: JJA temperature comparison between paleoclimate reconstructions Spatial maps showing the summer temperature (JJA) as deviation for each reconstruction from the ensemble mean (n = 4; refs.[30,31,32] and this study). Note, for ref.[30], this corresponds to the moderate temperature reconstruction.

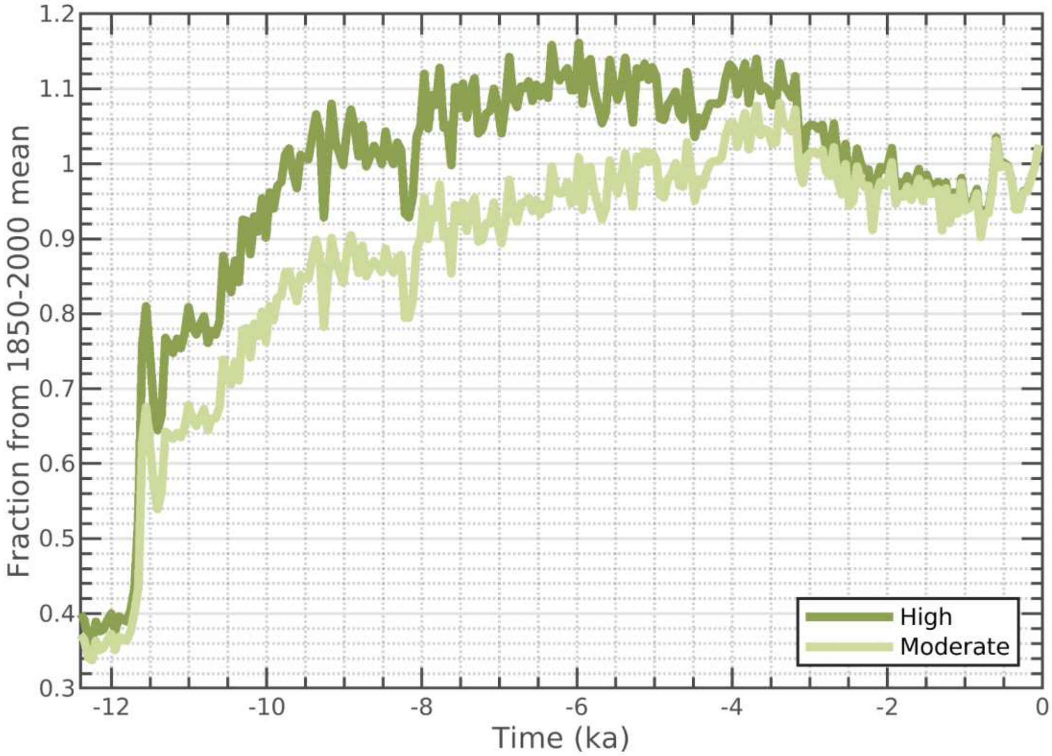

Extended Data Fig. 8: Reconstructed Holocene mean annual precipitation ratio
Reconstructed Holocene mean annual precipitation for ref.[30] expressed as fraction of precipitation from the 1850-2000 mean from ref.[69].

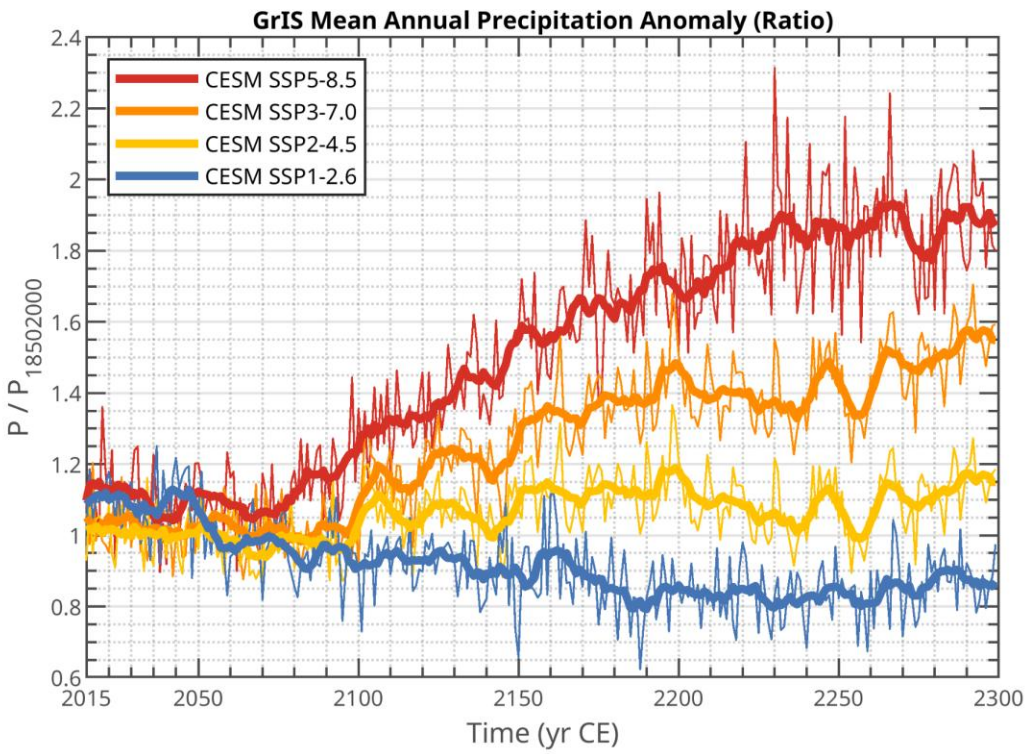

Extended Data Fig. 9: GrIS mean annual precipitation ratio for all 4 SSP scenarios
Future mean annual precipitation expressed as an anomaly ratio from the mean 1850-2000 CE period, shown as the yearly component (thin line) and 10-point running mean (thick bold line) for each SSP scenario.

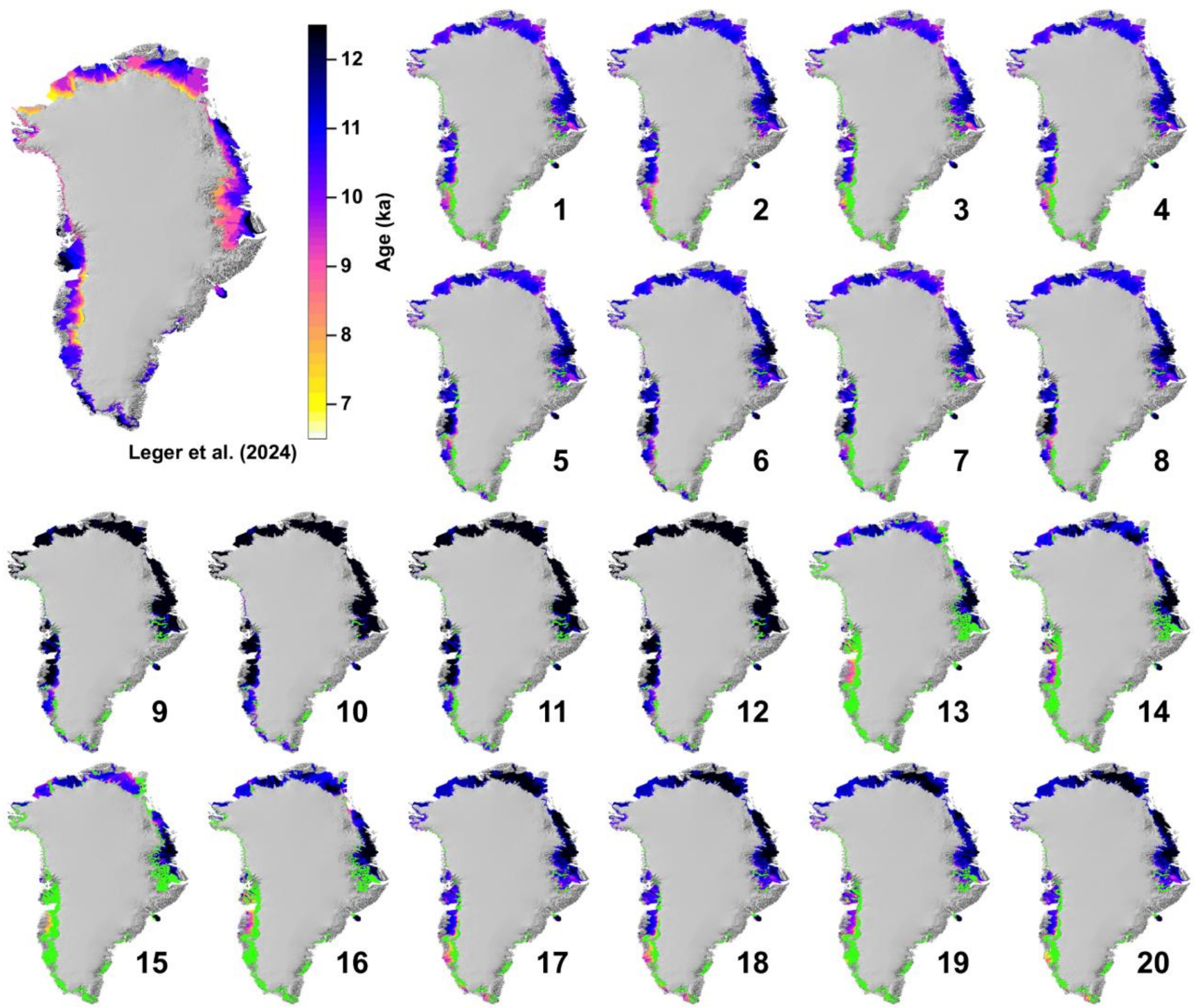

Extended Data Fig. 10: DMC-1 comparison maps

Summary maps of Holocene GrIS deglaciation results from each of the ensemble members against the observational product from ref.[28]. The number for each simulation corresponds to the summary Extended Data Table 2. Note the bright green pixels in each simulation result that demonstrate where there are missing deglacial pixels from the simulation compared to the observational product from ref.[28]. Because the simulations use the 12.5 ka isochron from ref.[28] as the starting position, missing pixels indicate either the persistence of the ice sheet in those locations after 6.5 ka or excessive re-growth of the ice sheet during the Little Ice Age.

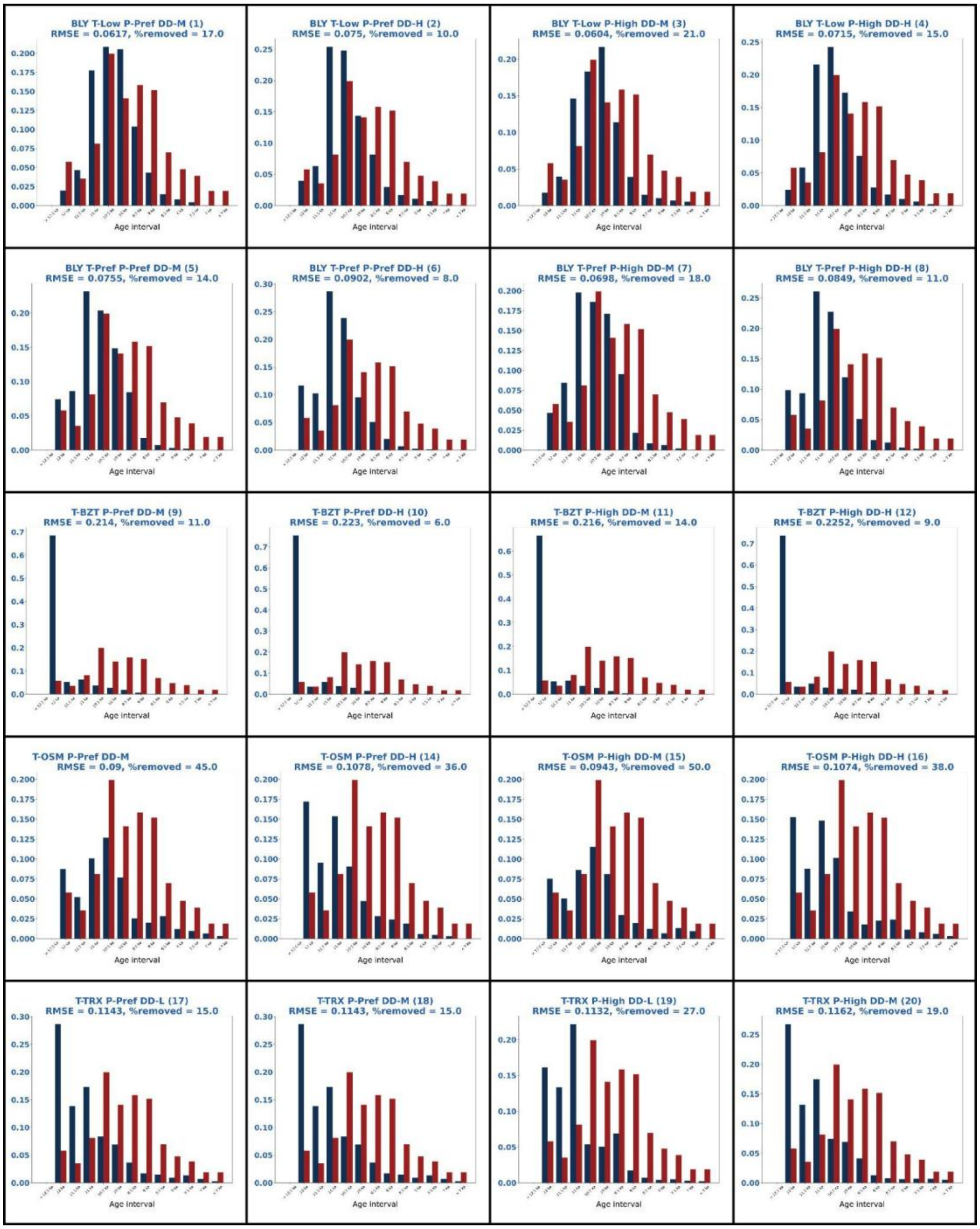

Extended Data Fig. 11: DMC-1 comparison, summary histograms

Bar plots demonstrating the proportion of the ice sheet deglaciated at each time step. The y-axis for each plot is in % deglaciated. Red bars represent the proportion of deglaciated pixels at each time step in the observational product from ref. [28], and dark blue bars represent the proportion of deglaciated pixels at each time step in each of the ensemble simulations. Numbers in each plot header correspond to the ensemble simulation number in Extended Data Table 1. We report the summary RMSE value and the percentage of pixels missing from each ensemble simulation relative to the observational product[28] (e.g., the percentage of all pixels in each simulation represented by the bright green color in Extended Data Fig. 10).

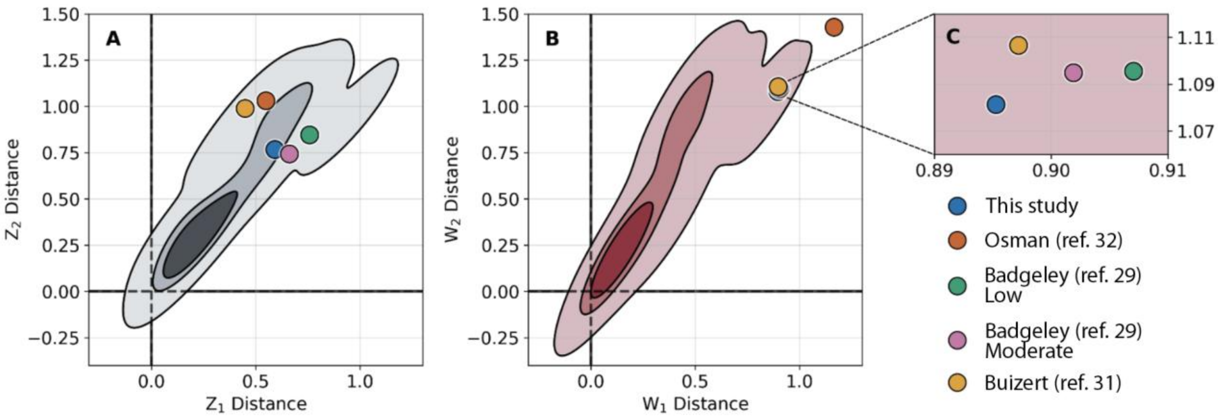

Extended Data Fig. 12: DMC-2 paleoclimate reconstruction comparison

Pairwise Procrustes distances for (A) temporal factor scores, Z_1 and Z_2, as well as (B) temporal loadings, W_1 and W_2, for each temperature reconstruction relative to the full proxy-network reference solution (circles). An inset (C) of panel B is included to distinguish overlapping spatial solutions of four reconstructions. Shaded regions denote the null distributions of Z and W distances determined by Monte Carlo resampling of the proxy network, with light, medium, and dark shading illustrating the 99^{th}, 68^{th}, and 34^{th} percentiles, respectively.

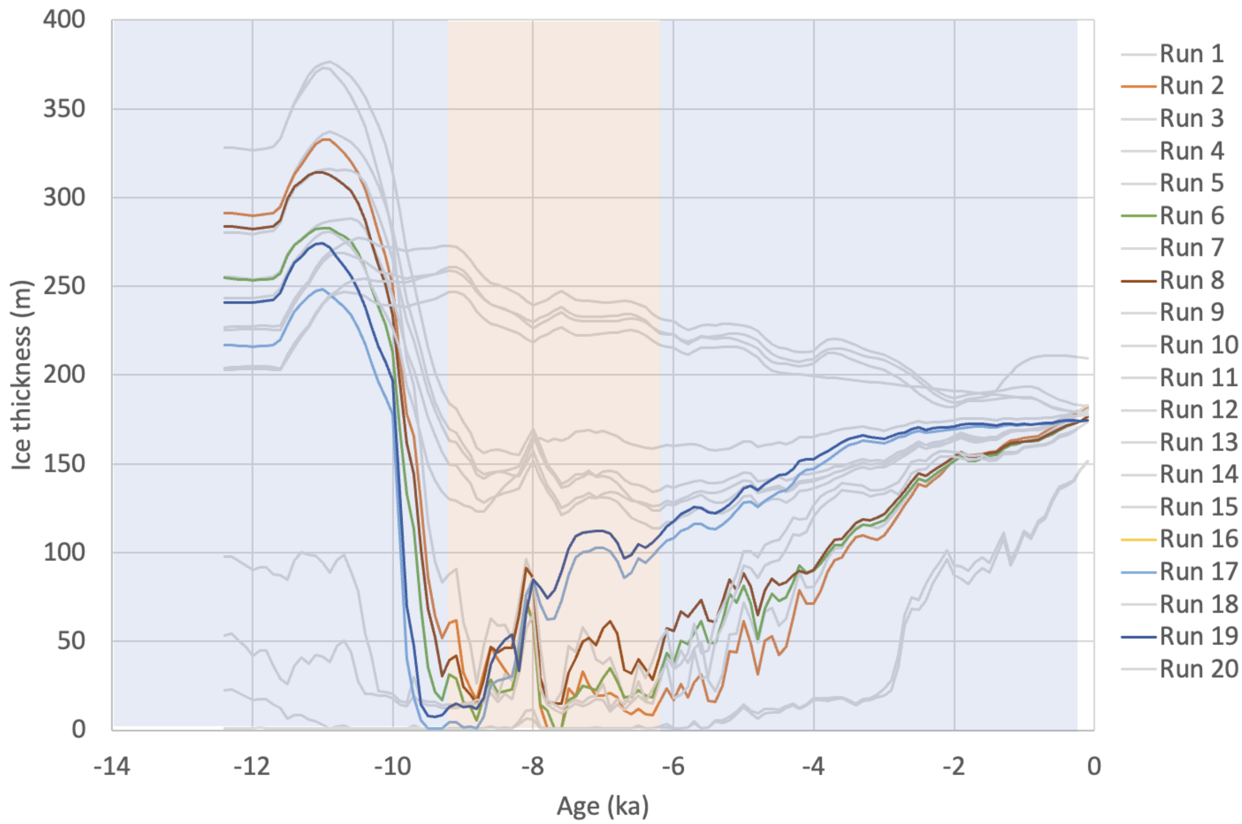

Extended Data Fig. 13: DMC-4 comparison of Prudhoe Dome absence
Simulated ice thickness evolution at the center of Prudhoe Dome, NW Greenland. The blue-salmon-blue color pattern denotes when observational data suggest Prudhoe Dome existed (blue) versus absent (salmon) during the Holocene. Runs denoted by a colored line are those that have a simulated ice-thickness history that is compatible with the observational data[75], thereby passing this criterion.

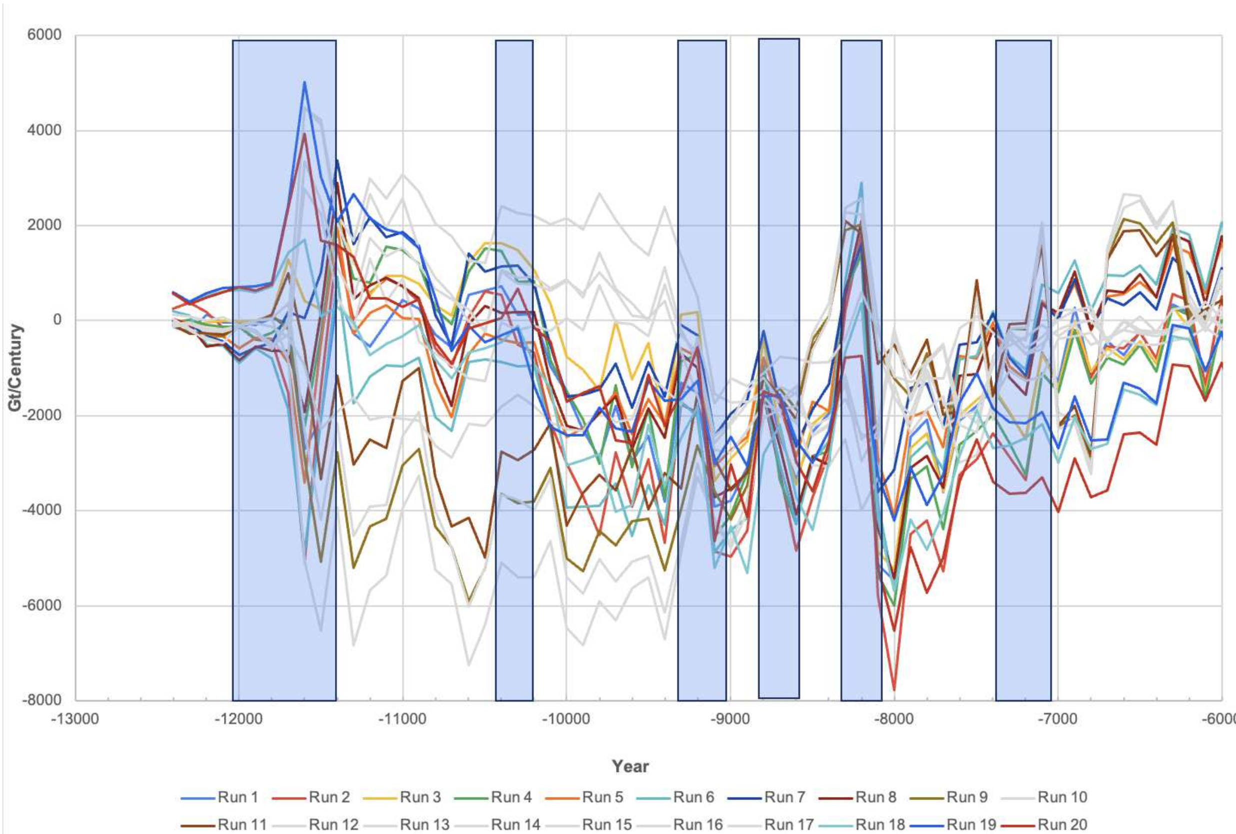

Extended Data Fig. 14: DMC-5 SW Greenland moraine pulsebeats
Gt/Century trends for the SW+CW domains in which refs.[73,74] dated six widely-traced moraines that record pulsebeat behavior of GrIS evolution superimposed on net ice-recession during the early and middle Holocene. Colored lines are those runs that exhibit consistent behavior with these six moraine formations, thereby passing this criterion.

Run #	Climate Forcing: Temperature	Climate Forcing: Precipitation	Oceanic Forcing	Degree Day Forcing	Result of Data-model comparison (DMC)
1	Badgeley low	Badgeley moderate	ECCO Climatology (1992-2015)	Medium	Not Selected
2	Badgeley low	Badgeley moderate	ECCO Climatology (1992-2015)	High	Pass
3	Badgeley low	Badgeley high	ECCO Climatology (1992-2015)	Medium	Not Selected
4	Badgeley low	Badgeley high	ECCO Climatology (1992-2015)	High	Pass
5	Badgeley moderate	Badgeley moderate	ECCO Climatology (1992-2015)	Medium	Not Selected
6	Badgeley moderate	Badgeley moderate	ECCO Climatology (1992-2015)	High	Pass
7	Badgeley moderate	Badgeley high	ECCO Climatology (1992-2015)	Medium	Not Selected
8	Badgeley moderate	Badgeley high	ECCO Climatology (1992-2015)	High	Pass
9	Buizert	Badgeley moderate	ECCO Climatology (1992-2015)	Medium	Not Selected
10	Buizert	Badgeley moderate	ECCO Climatology (1992-2015)	High	Not Selected
11	Buizert	Badgeley high	ECCO Climatology (1992-2015)	Medium	Not Selected
12	Buizert	Badgeley high	ECCO Climatology (1992-2015)	High	Not Selected
13	Osman	Badgeley moderate	ECCO Climatology (1992-2015)	Medium	Not Selected
14	Osman	Badgeley moderate	ECCO Climatology (1992-2015)	High	Not Selected
15	Osman	Badgeley high	ECCO Climatology (1992-2015)	Medium	Not Selected
16	Osman	Badgeley high	ECCO Climatology (1992-2015)	High	Not Selected
17	This study	Badgeley moderate	ECCO Climatology (1992-2015)	Low	Not Selected
18	This study	Badgeley moderate	ECCO Climatology (1992-2015)	Medium	Pass
19	This study	Badgeley high	ECCO Climatology (1992-2015)	Low	Not Selected
20	This study	Badgeley high	ECCO Climatology (1992-2015)	Medium	Pass

Temperature Scenarios

Badgeley et al. (ref. 29)
Buizert et al. (ref. 31)
Osman et al. (ref. 32)
This study

Precipitation Scenarios

Badgeley et al. (ref. 29)

Other Boundary Conditions

GIA	Prescribed from ref. 44
Submarine Melt	PICOP (ref. 60)
Moving Front	Calving stress thresholds from ref. 52
Oceanic Temp. and Salinity	Constant temperature and salinity forcing (ECCO climatology, 1992–2015), Shelf depth (400-450 m), ref. 61
Friction	Transient adjustment of Fric. Coeff. following ref. 41

Degree Day Scenario (mm/day °C)

Medium	Medium (snow = 3, ice = 6 mm d^{-1} $°C^{-1}$)
High	High (snow = 4.3, ice = 8.3 mm d^{-1} $°C^{-1}$)

Extended Data Table 1: Summary of ice sheet model simulations

List of Holocene simulations. The summary of model simulations performed in this study is listed with the respective boundary conditions and parameterizations used.

run number	1	2	3	4	5	6	7	8	9	10	11	12	13	14	15	16	17	18	19	20
PaleoGrIS matching	1	1	1	1	1	1	1	1	0	0	0	0	1	0	1	0	0	0	0	0
Climate forcing	1	1	1	1	1	1	1	1	1	1	1	1	0	0	0	0	1	1	1	1
Present day target	0	1	0	1	0	1	0	1	1	1	1	1	0	0	0	0	0	1	0	1
Ice free Prudhoe Dome	0	1	0	1	0	1	0	1	1	1	1	1	0	0	0	0	0	1	0	1
Pulsebeat moraine record matching	1	1	1	1	1	1	1	1	1	0	1	0	0	0	0	0	0	1	1	1
Mid Holocene area minimum	1	1	1	1	1	1	1	1	1	1	1	1	0	0	0	0	1	1	1	1
Ice Area 13-7 ka compared to PaleoGrIS	1	1	0	1	1	1	1	1	0	0	0	0	0	0	0	0	1	1	1	1
total	**5**	**7**	**4**	**7**	**5**	**7**	**5**	**7**	**5**	**4**	**5**	**4**	**1**	**0**	**1**	**0**	**3**	**6**	**4**	**6**

Extended Data Table 2: Summary of Data-model comparison results

Results of our DMC. Table showing the results of how each of our 20 model simulations evaluated against the seven data-model comparison (DMC) criteria. Highlighted in green are the simulations which passed our DMC.

Supplementary Information

Supplementary Note 1: Elevation Corrections for Paleoclimate Reconstructions

During the deglaciation the GrIS was substantially larger and thicker than today, and the temperature reconstructions we use represent conditions over the ice sheet as it existed at different points in time. As the margins retreated — particularly in low-elevation coastal regions — the areal extent and surface elevation of the ice sheet changed considerably, and these evolving geometric differences impact our climate forcings. The model prior in all the reconstructions uses the ice-sheet history from Ice6G[1], but this is treated in different ways. For ref.[2], the prior is static, drawing from an ensemble of TraCE-21ka 20–0 ka simulations, and therefore represents temperatures over an average paleo-elevation of the GrIS. In ref.[3], the prior evolves through time following Ice6G (as in ref.[4]), and no correction for elevation is applied; note that ref.[3] assimilates no ice-core data. In ref.[4], and in our new reconstruction, elevations are lapse-rate corrected from Ice6G so that they are referenced relative to the modern GrIS (ref.[4] uses 5˚C/km; in our reconstruction we use 6˚C/km for consistency with our ice sheet modeling). In our reconstruction, we additionally include uncertainty in elevation as part of the observation error covariance term, R, in the assimilation framework following ref.[5]. For interior sites with relatively stable topography over the Holocene, we assign an additional temperature uncertainty of 1.2 °C (on top of other sources of error), corresponding to 200 m of elevation uncertainty. For coastal sites, which experienced greater paleo-elevation change[6], and are therefore less likely to be as well represented by the prior, we use a greater uncertainty of 2.4 °C.

Supplementary Note 2: Future temperature and precipitation extensions to 2300 CE

Temperature extensions to 2300 CE

Annual global-mean surface air temperature anomalies (relative to 1850–2000 CE) were computed from CESM2-WACCM output and smoothed using a 5-year running mean to reduce high-frequency variability. A least-squares linear fit to the smoothed 2070–2099 CE global-mean temperature anomalies were used to estimate the late-century warming rate. This trend was extrapolated beyond 2100 CE and smoothly transitioned toward a bounded 2300 CE target. Because SSP2-4.5 and SSP3-7.0 simulations terminate at 2100 CE, the terminal global-mean anomaly was constrained to fall within the envelope defined by the extended low- and high-forcing pathways (SSP1-2.6 and SSP5-8.5). Specifically, the late-century (upper decile) mean anomalies from these scenarios were used to define lower and upper bounds, and the 2300 CE target was set to an intermediate value between them. A smooth logistic transition was applied between the extrapolated late-century trend and the 2300 target to avoid artificial inflection points or discontinuities. The extended global-mean temperature anomaly time series was then normalized by the late-century warming amplitude to produce a dimensionless climate index I(t), which was used to scale the spatial warming pattern in the pattern-scaling framework described below.

To reconstruct spatial temperature fields beyond 2100 CE, we adopted a pattern-scaling approach[7] in which the spatial structure of late-century CESM2-WACCM warming is preserved while its amplitude evolves according to the extended global-mean temperature trajectory. The spatial warming pattern $\Delta T_{unit}(x)$ was computed from the CESM simulation as the difference between mean temperature anomaly fields averaged over the final decade of the simulation (2091–2099 CE) and a broader late-century climatology (2069–2099 CE). This difference represents the spatial pattern of incremental late-century warming.

Future monthly temperature anomaly fields were then generated as:

$$T(x,t) = T_{base}(x) + I(t)\,\Delta T_{unit}(x)$$

where $T_{base}(x)$ is the late-century baseline anomaly field (2069–2099 CE), $\Delta T_{unit}(x)$ is the spatial pattern of incremental late-century warming derived from the CESM simulation, and $I(t)$ is a normalized global climate index derived from the extended global-mean temperature anomaly time series. This formulation preserves the CESM-simulated spatial structure of warming while scaling its magnitude according to the extended global trajectory.

Because the climate index $I(t)$ is derived from the global annual-mean temperature anomaly, the seasonal structure of the CESM temperature and precipitation fields is assumed to remain constant beyond 2100. Monthly anomalies therefore evolve through amplitude scaling of the diagnosed late-century spatial patterns while retaining the seasonal cycle simulated by CESM2-WACCM.

Interannual variability beyond 2100 was generated using a spatially heterogeneous AR(1) process where ϵ_t is the stochastic anomaly

$$\epsilon_t = \phi\epsilon_{t-1} + \sqrt{1-\phi^2}\,\sigma(x)\,\eta_t,$$

and where $\phi = 0.4$, $\sigma(x)$ is the standard deviation from the final 30 years of CESM output, and η_t is Gaussian white noise. A partially coherent domain-wide component was superimposed to represent large-scale variability shared across the ice sheet and the seasonal cycle from late-century CESM output was retained.

In total, by extending the SSP2-4.5 and SSP3-7.0 temperature trajectories to 2300 CE, the resulting set of forcings represents a range of plausible warming pathways that the GrIS may experience. The extended scenarios, together with the CESM2-WACCM simulations that already extend to 2300 CE (SSP1-2.6 and SSP5-8.5), span a broad range of future temperature anomalies. When averaged over the GrIS (Extended Data Fig. 1), annual mean temperature anomalies relative to the 1850–2000 CE mean reach approximately ~16 °C for SSP5-8.5, ~10 °C for SSP3-7.0, ~5.5 °C for SSP2-4.5, and ~0.5 °C for SSP1-2.6 by 2300 CE. For the SSP5-8.5, SSP3-7.0, and SSP2-4.5 scenarios, peak warming occurs toward the end of the 22nd century, after which temperatures stabilize. In contrast, SSP1-2.6 peaks around 2050 CE before gradually cooling and stabilizing.

Precipitation extensions to 2300 CE

Precipitation anomalies were treated as ratio anomalies relative to the 1850–2000 CE mean (i.e., P divided by the 1850–2000 mean). Annual global-mean precipitation ratios were smoothed using a 5-year running mean. Because long-term precipitation projections under SSP2-4.5 and SSP3-7.0 are not available beyond 2100 CE, we imposed a physically bounded exponential relaxation from the 2099 value toward a prescribed long-term target increase, with targets of 25% for SSP2-4.5 and 50% for SSP3-7.0 by 2300 CE, consistent with their relative warming. This range is consistent with 21st-century projections and thermodynamic scaling of precipitation with warming (~2–3% per °C globally; ref.[8]), as well as higher Greenland-specific sensitivities (~5% per °C; ref.[9]), which together imply substantial cumulative increases under sustained warming. The extended annual trajectory was constructed as:

$$P(t) = P\_2099 + (P\_target - P\_2099) \times (1 - \exp(-(t - 2100)/\tau))$$

where P_2099 is the precipitation ratio at 2099, P_target is the prescribed long-term precipitation ratio corresponding to scenario specific increases of 25% (SSP2-4.5) and 50% (SSP3-7.0) relative to the 1850–2000 baseline, t is time in years, and $\tau = 180$ years is the e-folding timescale controlling the rate of adjustment. This formulation ensures a smooth, monotonic transition beginning at 2100 CE and asymptotically approaching the prescribed target, without introducing artificial acceleration or discontinuities (Extended Data Fig. 9).

Beyond 2100 CE, regional precipitation anomalies were obtained by scaling the late-century CESM spatial pattern with the evolving global-mean precipitation anomaly, analogous to the temperature pattern-scaling approach, while retaining the seasonal cycle from the model. Interannual variability was represented using a spatially heterogeneous AR(1) process ($\varphi = 0.3$) with reduced variance relative to temperature anomalies.

Supplementary Note 3: Data-model comparison (DMC) descriptions

DMC-1: Timing and patterns of ice margin retreat simulated versus observed

We take advantage of the recently published PaleoGRIS product of spatiotemporal Holocene GrIS margin retreat[10] to compare with each of our ISSM simulated Holocene GrIS histories (Fig. 1). We use raster representations of simulated (ISSM) versus observed GrIS Holocene retreat histories[10] at 1.5 km scale resolution. Each raster pixel in both the observational layer and the ISSM simulated layers contains a numeric value that represents the timing of deglaciation of that pixel. For the observational product from ref.[10], all pixels that are at or within a mapped limit get assigned that limit's deglaciation age. For example, the areas between two delineated ice margins get assigned a deglaciation age of the outermost limit, treating mapped ice margins essentially as maximum constraints. For the ISSM simulations, each pixel contains a deglaciation age as determined by the simulation, although as described below, through the comparison workflow, simulated deglaciation ages get binned at a 500-yr temporal resolution to be consistent with the temporal resolution of the observational layer.

To make each comparison between the observational layer and each simulated ice-margin history in the ensemble, we take a holistic approach rather than evaluating model results against observations at each individual pixel. The aim is to compare if model simulations capture the general trend of ice margin retreat as opposed to matching observations exactly. The workflow for comparing each simulated ISSM output is as follows.

First, we sum up the total number of pixels for each 500 yr time step in the observational layer and divide that by the total number of pixels representing deglaciation over the entire deglacial interval. In the case of this comparison, that total interval spans 12.5 ka to 6.5 ka. See maps in Extended Data Fig. 10 and histograms in Extended Data Fig. 11 for examples.

Next, we calculate a summary root-mean-square error (RMSE) value that represents the average percent difference between the proportion of deglaciated pixels in the observational layer and a simulated result at each time interval. To incur an additional penalty for our comparison, we take into account the absence of a proportion of pixels that should be represented with a deglaciation value in each ISSM simulated result - according to the observational layer - but which are not represented. These pixels that should have deglaciation values but are essentially missing and not represented in a given simulated result are highlighted in bright green on Extended Data Fig. 10. We calculate the proportion of absent pixels in each simulated result and scale each RMSE by that ‘missing’ proportion. Thus, if a simulated result appears to follow the same general spatiotemporal trend of the observed deglaciation and has a good RMSE value, but a high proportion of the observational layer is missing in the comparison due to poor spatial overlap between the two products, that mismatch is better-represented and the simulation is more heavily penalized, significantly increasing the “corrected” RMSE we use for our comparison metric.

Finally, we use a cut-off “corrected” RMSE value of 0.10 as our binary metric for pass versus failure in this portion of the data model comparison. The results are displayed in Fig. S11, and demonstrate that the ISSM simulations that use climate forcing from ref.[4] and this study most frequently pass this DMC criteria, although two of the simulations that use climate forcing from ref.[3] pass this DMC criteria as well. As a complete example, ISSM simulation Run 1 (Map results in Extended Data Fig. 10 denoted with a 1 and histogram results in Extended Data Fig. 11 denoted with the 1 in the plot title of the top row, leftmost chart), indicates that 17% of the pixels from the observational product[10] were not represented in Run 1 (note the green pixels in the map plot mostly concentrated in the S-SW portion of the ice sheet), but the resulting RMSE (with the 17% penalty incurred) is 0.0617. Thus, Run 1 passes the first data-model comparison criterion (see Extended Data Table 2) since the summary RMSE is below our 0.10 binary metric.

DMC-2: Comparisons of proxy and climate reconstructions

We compiled 27 independent and previously published quantitative summer temperature time series (refs.[11-35]). We restricted time-series selection to include only proxies that are sensitive to summer temperatures, and which were not used in the development of our climate-forcing reconstructions. To improve spatial coverage in northern Greenland, we supplemented the quantitative records with 11 previously reported time series of qualitative summer temperature (refs.[35-45]). To incorporate the qualitative time series into this analysis, we categorized the original author's climatic interpretations into categories: *coldest, cold, warm,* and *warmest,* where the extremes are incorporated if identified in the original work. These categories were then converted to numerical values, -1.5, -0.5, 0.5, and 1.5, respectively, assuming equal spacing between qualitative categories. We assign an uncertainty of 1.0 to these semi-quantitative time series, assuming uncertainty equivalent to one category. For all 38 time series, we applied a cascading time-binning strategy in which observations were first aggregated into 50-year time bins and then into 200 year bins, to avoid potentially biasing binned observations by high-density clusters of observations in the original time series.

We assess the agreement between the five climate reconstructions and proxy observations through a two-stage process. The first stage uses a probabilistically resolved Factor Analysis (FA) to individually decompose the proxy time series and reconstructions, identifying dominant climate modes within the records. We configure the FA similarly to a probabilistic principal component analysis (pPCA; ref.[46]). Our implementation of the FA differs from the pPCA through our defined error term. Where the pPCA assumes isotropic error, assuming an equal and shared error for each vector in the analysis (ref.[46]), we define an anisotropic error term, realized using uncertainties from the proxy-temperature transfer functions used to quantitatively interpret the time series. Ultimately, this error configuration incorporates proxy confidence by inversely weighting the influence of a given proxy time series based on proxy-specific uncertainties, resolving known issues of variance weighting in similar signal decomposition approaches (e.g., refs.[47.48]). Finally, a varimax rotation was applied[47] to improve interpretability. The FA solutions yield information on temporal and spatial trends within the data.

For each reconstruction (refs.[2,3,4] and this study) we computed mean summer temperatures (June, July, and August) for each grid cell. We then applied the same time-binning approach as we did to the proxy network. To achieve an equitable spatial comparison between the reconstructions and the proxy-network, we isolated reconstruction grid cells that overlapped with proxy time series. For the temporal comparison, we only consider time bins that overlap with observations in the binned proxy time series for overlapping proxy and reconstruction grid cells. Where more than one time series overlaps with a grid cell, we use the combined proxy time series observations to temporally subset the paired grid cell.

The temporally and spatially aligned proxy time series and reconstructions were z-scored to normalize variance through time. Normalization is commonly used in dimension-reduction analyses to dampen the influence of high variance within the dataset that can skew the extracted signal. Moreover, normalization is critical to this work as it enables the incorporation of different proxy measurements. Although most records are reported in degrees Celsius, we also include a chlorophyll record[49], and 11 qualitative time series in northern Greenland.

The second stage of the comparison uses Procrustes least-squares analysis[50] to quantify the similarity of decomposed temporal and spatial climate patterns between the proxy networks and the reconstructions. Transformations were restricted to preserve valid temporal and spatial comparisons. Temporal scores and spatial loadings (Z and W, respectively) could be sign-inverted, reflecting the arbitrary sign convention of factor-analysis solutions; however, the sign inversion of W was coupled to sign inversion of the corresponding Z score. Scaling of Z and W solutions had a lower bound of 0.3 to avoid potentially muting solutions to improve comparisons. Factor solutions were only compared within corresponding components (i.e., component 1 of the proxy could only be compared to component 1 of the reconstruction), and we did not allow scaling or inversion of the time axis. Similarity was quantified using Procrustes sum-of-squared residuals after alignment.

To assess whether agreement between the proxy network and reconstructions exceeds variability expected from proxy-network composition, we constructed a proxy bootstrap null distribution using Monte Carlo resampling. We generated 100 realizations of the proxy network by randomly retaining 65% of proxy records and repeating the FA for each subset. For each bootstrap realization, the temporal scores and spatial loadings (Z_1, Z_2, W_1, and W_2) were aligned to the full proxy-network solution using the same constrained Procrustes procedure described above. This distribution provides a baseline against which agreement between the proxy network and reconstruction can be evaluated. We then calculated the mean Procrustes distances of Z_1, Z_2, W_1, and W_2 between each reconstruction and the full proxy-network solution and compared these values to the bootstrap distribution (Extended Data Fig. 12). Distances for refs.[2,4] and this study reconstructions fall within the 99^{th} percentile of the proxy bootstrap distributions of both Z and W solutions, indicating agreement with the proxy-derived climate modes[50]. In contrast, reconstruction of ref.[3] exceeds the 99^{th} percentile threshold of both spatial loadings, W_1 and W_2, suggesting weaker consistency with the proxy network.

DMC-3: Total GrIS area simulated versus observed

We also leverage PaleoGRIS[10] to capture the agreement between simulated and observed whole-GrIS area change (Fig 1B.). While we acknowledge uncertainty in the age control and position of PaleoGRIS boundaries, it provides an overall state-of-the-art constraint on area changes of the GrIS in 11 500-year time increments from 12 ka to 7 ka. For each of our 20 simulations, we calculated the area in each time increment to compare with PaleoGRIS. For this criterion, we deem a good data-model fit when agreement is within 10% and score simulations with a one if nine or more of the 11 time slices have a mismatch of 10% or lower. If the mismatch is 10% or greater in more than two of the 11 time slices, then the simulation earns a zero.

DMC-4: Prudhoe Dome absence in middle Holocene

Ref.[51] recently demonstrated that Prudhoe Dome, a 500-m-thick spur of the GrIS in Northwest Greenland, was absent sometime between ~9 and 7.1±1.1 ka. This is a one-of-a-kind dataset where Holocene absence/presence is detected far inland and through relatively thick ice, which provides a tighter constraint on Holocene minimum size that more typical methods able to assess re-advances very near the GrIS margins (see DMC-6). We use this finding to evaluate simulated ice-thickness history through the Holocene at the center of Prudhoe Dome and score individual simulations if they become ice-free (simulated thickness of 10 m or less) during this window (Extended Data Fig. 13). If they become ice free before this time window, or remain ice free after this time window, they are scored a zero. If on the other hand they become ice-free and then re-grow during this time window, then they are scored a one.

DMC-5: SW Greenland moraine pulsebeats

Following ref.[52], we use the well-dated moraine record in SW Greenland[53] to evaluate simulated mass balance (Gt/century) trends in the SW domain of our model space (Extended Data Fig. 14). The wide area of unglaciated terrain in SW Greenland contains six well-dated moraines at roughly millennial pacing that would have required reversals or plateaus in mass balance superimposed on overall negative mass balance. We assess the simulated Gt/century trends of each individual simulation against the timing of widespread moraine formation. We assign a value of one to any simulation that displays a characteristic mass balance reversal (or pause followed by a significant decrease in mass balance) for 3 or more of the 6 time intervals.

DMC-6: Whole-GrIS Holocene minimum extent

Abundant evidence from around the entire perimeter of the GrIS reveals a Holocene minimum extent followed by expansion toward the historical maximum ice margin[53]. We note however that some individual simulations do not show a minimum extent in GrIS area whereas others do. For this criterion, we simply give simulations a one if they exhibit a minimum phase followed by re-expansion and a zero if they do not (Fig. 1B).

DMC-7: Present-day GrIS area simulated versus observed

For this criterion we compare the ending simulation in 1850 CE with the modern-day observed GrIS area (initialized in ISSM at 1.75 million km^2). We acknowledge that in reality the GrIS to some degree covered more area at 1850 CE, during the Little Ice Age (or what on Greenland is referred to as its historical extent), than today. One recent estimate is that the GrIS covered 1% more area[54]. In any case, we score our simulations with one if they agree within 10% of the modern GrIS area.

Supplementary References

1. W.R. Peltier, D. F. Argus, R. Drummond, Space geodesy constrains ice age terminal deglaciation: The global ICE-6G_C (VM5a) model. Journal of Geophysical Research: *Solid Earth,* **120**(1), 450-487 (2015).

2. Buizert, C., Keisling, B. A., Box, J. E., He, F., Carlson, A. E., Sinclair, G. & DeConto, R. M. Greenland-wide seasonal temperatures during the last deglaciation. *Geophys. Res. Lett.* **45**, 1905–1914 (2018).

3. Osman, M. B., Tierney, J. E., Zhu, J., Tardif, R., Hakim, G. J., King, J. & Poulsen, C. J. Globally resolved surface temperatures since the Last Glacial Maximum. *Nature* **599**, 239–244 (

4. Badgeley, J. A., Steig, E. J., Hakim, G. J. & Fudge, T. J. Greenland temperature and precipitation over the last 20,000 years using data assimilation. *Clim. Past* **16**, 1325–1346 (2020).

5. Hakim, G. J., Emile-Geay, J., Steiger, W. J. & Noone, D. M. Last Millennium Climate Reanalysis project: Framework and first results. *J. Geophys. Res. Atmos.* **121**, 6745–6764 (2016).

6. Vinther, B. M., Buchardt, S. L., Clausen, H. B., Dahl-Jensen, D., Johnsen, S. J., Fisher, D. A., Koerner, R. M., Raynaud, D., Lipenkov, V., Andersen, K. K., Blunier, T., Rasmussen, S. O., Steffensen, J. P. & Svensson, A. M. Holocene thinning of the Greenland ice sheet. *Nature* 4**61**, 385–388 (2009).

7. T.D. Mitchell, Pattern scaling: An examination of the accuracy of the technique for describing future climates. *Clim. Change* **60**, 217–242 (2003).

8. Held, I. M. & Soden, B. J. Robust responses of the hydrological cycle to global warming. *J. Clim*. **19**, 5686–5699 (2006).

9. Boberg, F., Hansen, N., Mottram, R., Fettweis, X. & van den Broeke, M. R. 21st century change in precipitation on the Greenland Ice Sheet using high resolution regional climate models. Preprint at https://doi.org/10.5194/tc-20-2947-2026 (2025).

10. Leger, T. P. M., Clark, C. D., Huynh, C., Jones, S., Ely, J. C., Bradley, S. L., Diemont, C. & Hughes, A. L. C. A Greenland-wide empirical reconstruction of paleo ice sheet retreat informed by ice extent markers: PaleoGrIS version 1.0. *Clim. Past* **20**, 701–755 (2024).

11. Acharya, S., Cluett, A. A., Grogan, A. L., Briner, J. P., Castañeda, I. S. & Thomas, E. K. Holocene temperatures in southwestern Greenland controlled by topography, ice sheet proximity and oceanic conditions. Preprint at https://doi.org/10.5194/egusphere-2025-3113 (2025).

12. Schneider, T., Castañeda, I. S., Zhao, B., Krüger, S., Salacup, J. M. & Bradley, R. S. Tracing Holocene temperatures and human impact in a Greenlandic lake: Novel insights from hyperspectral imaging and lipid biomarkers. *Quat. Sci. Rev.* **339**, 108851 (2024).

13. Cluett, A. A., Thomas, E. K., McKay, N. P., Cowling, O. C., Castañeda, I. S. & Morrill, C. Lake dynamics modulate the air temperature variability recorded by sedimentary aquatic

biomarkers: A Holocene case study from western Greenland. *J. Geophys. Res. Biogeosci.* **128**, e2022JG007106 (2023).

14. Harning, D. J., Curtin, L., Geirsdóttir, Á., D'Andrea, W. J., Miller, G. H. & Sepúlveda, J. Lipid biomarkers quantify Holocene summer temperature and ice cap sensitivity in Icelandic lakes. *Geophys. Res. Lett.* **47**, e2019GL085728 (2020).

15. Axford, Y., Lasher, G. E., Kelly, M. A., Osterberg, E. C., Landis, J. & Schellinger, G. C. Holocene temperature history of northwest Greenland with new ice cap constraints and chironomid assemblages from Deltasø. *Quat. Sci. Rev.* **215**, 160–172 (2019).

16. Caron, M., Rochon, A., Montero-Serrano, J.-C. & St-Onge, G. Evolution of sea-surface conditions on the northwestern Greenland margin during the Holocene. *J. Quat. Sci.* **34**, 569–580 (2019).

17. Axford, Y., Levy, L. B., Kelly, M. A., Francis, D. R., Hall, B. L., Langdon, P. G. & Lowell, T. V. Timing and magnitude of early to middle Holocene warming in East Greenland inferred from chironomids. *Boreas* **46**, 678–687 (2017).

18. Van Nieuwenhove, N., Baumann, A., Matthiessen, J., Bonnet, S. & de Vernal, A. Sea surface conditions in the southern Nordic Seas during the Holocene based on dinoflagellate cyst assemblages. *Holocene* **26**, 722–735 (2016).

19. Gibb, O. T., Steinhauer, S., Fréchette, B., de Vernal, A. & Hillaire-Marcel, C. Diachronous evolution of sea surface conditions in the Labrador Sea and Baffin Bay since the last deglaciation. *Holocene* **25**, 1882–1897 (2015).

20. Ouellet-Bernier, M.-M., de Vernal, A., Hillaire-Marcel, C. & Moros, M. Paleoceanographic changes in the Disko Bugt area, West Greenland, during the Holocene. *Holocene* **24**, 1573–1583 (2014).

21. Sundqvist, H. S., Kaufman, D. S., McKay, N. P., Balascio, N. L., Briner, J. P. & Cwynar, L. C. Arctic Holocene proxy climate database: New approaches to assessing geochronological accuracy and encoding climate variables. *Clim. Past* **10**, 1605–1631 (2014).

22. Axford, Y., Losee, S., Briner, J. P., Francis, D. R., Langdon, P. G. & Walker, I. R. Holocene temperature history at the western Greenland Ice Sheet margin reconstructed from lake sediments. *Quat. Sci. Rev.* **59**, 87–100 (2013).

23. de Vernal, A., Hillaire-Marcel, C., Rochon, A., Fréchette, B., Henry, M., Solignac, S. & Bonnet, S. Dinocyst-based reconstructions of sea ice cover concentration during the

Holocene in the Arctic Ocean, the northern North Atlantic Ocean and its adjacent seas. *Quat. Sci. Rev.* **79**, 111–121 (2013).

24. von Gunten, L., D'Andrea, W. J., Bradley, R. S. & Huang, Y. Proxy-to-proxy calibration: Increasing the temporal resolution of quantitative climate reconstructions. *Sci. Rep.* **2**, 609 (2012).

25. D'Andrea, W. J., Huang, Y., Fritz, S. C. & Anderson, N. J. Abrupt Holocene climate change as an important factor for human migration in West Greenland. *Proc. Natl. Acad. Sci. U.S.A.* **108**, 9765–9769 (2011).

26. Fréchette, B. & de Vernal, A. Relationship between Holocene climate variations over southern Greenland and eastern Baffin Island and synoptic circulation pattern. *Clim. Past* **5**, 347–359 (2009).

27. Justwan, A., Koç, N. & Jennings, A. E. Evolution of the Irminger and East Icelandic Current systems through the Holocene, revealed by diatom-based sea surface temperature reconstructions. *Quat. Sci. Rev.* **27**, 1571–1582 (2008).

28. Solignac, S., Giraudeau, J. & de Vernal, A. Holocene sea surface conditions in the western North Atlantic: Spatial and temporal heterogeneities. *Paleoceanography* **21** (2006).

29. de Vernal, A. & Hillaire-Marcel, C. Provincialism in trends and high frequency changes in the northwest North Atlantic during the Holocene. *Glob. Planet. Change* **54**, 263–290 (2006).

30. Miller, G. H., Wolfe, A. P., Briner, J. P., Sauer, P. E. & Nesje, A. Holocene glaciation and climate evolution of Baffin Island, Arctic Canada. Quat. Sci. Rev. **24**, 1703–1721 (2005).

31. Kerwin, M. W., Overpeck, J. T., Webb, R. S. & Anderson, K. H. Pollen-based summer temperature reconstructions for the eastern Canadian boreal forest, subarctic, and Arctic. *Quat. Sci. Rev*. **23**, 1901–1924 (2004).

32. Kaplan, M. R., Wolfe, A. P. & Miller, G. H. Holocene environmental variability in southern Greenland inferred from lake sediments. *Quat. Res.* **58**, 149–159 (2002).

33. Levac, E., de Vernal, A. & Blake, W., Jr. Sea-surface conditions in northernmost Baffin Bay during the Holocene: Palynological evidence. *J. Quat. Sci.* **16**, 353–363 (2001).

34. Matthiessen, J. & Baumann, A. Dinoflagellate cyst records from the East Greenland continental margin during the last 15,000 years: Implications for palaeoceanographic reconstructions. In Micropaleontology and Paleoceanography from the Northern North

Atlantic (eds. Hass, C. & Kaminski, M.) 149–165 (Grzybowski Foundation Special Publication 5, 1997).

35. Wagner, B. & Bennike, O. Holocene environmental change in the Skallingen area, eastern North Greenland, based on a lacustrine record. *Boreas* **44**, 45–59 (2015).

36. Bennike, O. & Wagner, B. Deglaciation chronology, sea-level changes and environmental changes from Holocene lake sediments of Germania Havn Sø, Sabine Ø, northeast Greenland. *Quat. Res*. **78**, 103–109 (2012).

37. Schmidt, S., Wagner, B., Heiri, O., Klug, M., Bennike, O. & Melles, M. Chironomids as indicators of the Holocene climatic and environmental history of two lakes in Northeast Greenland. *Boreas* **40**, 116–130 (2011).

38. Klug, M., Schmidt, S., Bennike, O., Heiri, O., Melles, M. & Wagner, B. Lake sediments from Store Koldewey, Northeast Greenland, as archive of Late Pleistocene and Holocene climatic and environmental changes. *Boreas* **38**, 59–71 (2009).

39. Wagner, B., Bennike, O., Bos, J. A. A., Cremer, H., Lotter, A. F. & Melles, M. A multidisciplinary study of Holocene sediment records from Hjort Sø on Store Koldewey, Northeast Greenland. *J. Paleolimnol*. **39**, 381–398 (2008).

40. Bennike, O., Sørensen, M., Fredskild, B., Jacobsen, B. H., Böcher, J., Amsinck, S. L., Jeppesen, E., Andreasen, C., Christiansen, H. H. & Humlum, O. Late Quaternary Environmental and Cultural Changes in the Wollaston Forland Region, Northeast Greenland. In Advances in Ecological Research **40**, 45–79 (Elsevier, 2008).

41. Christiansen, H. H., Bennike, O., Böcher, J., Elberling, B., Humlum, O. & Jakobsen, B. H. Holocene environmental reconstruction from deltaic deposits in northeast Greenland. *J. Quat. Sci.* **17**, 145–160 (2002).

42. Bennike, O. Late Quaternary history of Washington Land, North Greenland. *Boreas* **31**, 260–272 (2002).

43. Bennike, O. & Weidick, A. Late Quaternary history around Nioghalvfjerdsfjorden and Jøkelbugten, North-East Greenland. *Boreas* **30**, 205–227 (2001).

44. Wagner, B., Melles, M., Hahne, J., Niessen, F. & Hubberten, H.-W. Holocene climate history of Geographical Society Ø, East Greenland—evidence from lake sediments. *Palaeogeogr. Palaeoclimatol. Palaeoecol.* **160**, 45–68 (2000).

45. Tipping, M. E. & Bishop, C. M. Probabilistic Principal Component Analysis. *J. R. Stat. Soc. Ser. B* **61**, 611–622 (1999).

46. Tierney, J. E., King, J., Osman, M. B., Abell, J. T., Burls, N. J., Erfani, E., Cooper, V. T. & Feng, R. Pliocene warmth and patterns of climate change inferred from paleoclimate data assimilation. *AGU Adv.* **6**, e2024AV001356 (2025).

47. Hong, Z., Long, D., Shan, K., Zhang, J.-M., Woolway, R. I., Liu, M., Mann, M. E. & Fang, H. Declining ocean greenness and phytoplankton blooms in low- to mid-latitudes under a warming climate. *Sci. Adv.* **11**, eadx4857 (2025).

48. Kaiser, H. F. The varimax criterion for analytic rotation in factor analysis. *Psychometrika* **23**, 187–200 (1958).

49. von Gunten, L., D'Andrea, W. J., Bradley, R. S. & Huang, Y. Proxy-to-proxy calibration: Increasing the temporal resolution of quantitative climate reconstructions. *Sci. Rep.* **2**, 609 (2012).

50. Schönemann, P. H. A generalized solution of the orthogonal Procrustes problem. *Psychometrika* **31**, 1–10 (1966).

51. Walcott-George, C. K., Brown, N. D., Briner, J. P., Balter-Kennedy, A., Young, N. E., Kuhl, T., Moravec, E., Anandakrishnan, S., Stevens, N. T., Keisling, B., DeConto, R. M., Gkinis, V., MacGregor, J. A. & Schaefer, J. M. Deglaciation of the Prudhoe Dome in northwestern Greenland in response to Holocene warming. *Nat. Geosci.* **19**, 189–194 (2026).

52. Briner, J. P., Cuzzone, J. K., Badgeley, J. A., Young, N. E., Morlighem, E. J., Schlegel, N.-J., Hakim, G. J., Schaefer, J. M., Lesnek, J. V., Thomas, E. K., Allan, E., Bennike, O., Cluett, A. A., Csatho, B., Downs, J., Larour, E. & Nowicki, S. Rate of mass loss from the Greenland Ice Sheet will exceed Holocene values this century. *Nature* **586**, 70–74 (2020).

53. Young, N. E., Briner, J. P., Miller, G. H., Lesnek, A. J., Crump, S. E., Thomas, E. K., Pendleton, S. L., Cuzzone, J., Lamp, J., Zimmerman, S., Caffee, M. & Schaefer, J. M. Deglaciation of the Greenland and Laurentide ice sheets interrupted by glacier advance during abrupt coolings. *Quat. Sci. Rev.* **229**, 106091 (2020).

54. Salmani, M., Csatho, B., Briner, J. P., Nowicki, S., Parmuzin, I., Eberhardt, H., Gao, H., Luzardi, A. C. & Talebigheshlaghi, G. Nearly half of Greenland's post-Little Ice Age area loss occurred since 2000. Preprint at https://doi.org/10.21203/rs.3.rs-9125064/v1 (2026).